Supplementary Information

The absolute chronology of Boker Tachtit (Israel) and implications for the Middle to Upper Paleolithic transition in the Levant

Elisabetta Boaretto, Marion Hernandez, Mae Goder-Goldberger, Vera Aldeias, Lior Regev, Valentina Caracuta, Shannon P. McPherron, Jean-Jacques Hublin, Steve Weiner, Omry Barzilai

SI-1. Stratigraphy

The sedimentation at Boker Tachtit is characterized by a succession of fine calcareous-rich laminations and beds that show substantial lateral variation with individual layers and lenses commonly pinching out across the profiles. Our stratigraphic subdivisions take into account major lithostratigraphic units (LU) based on large-scale sedimentological similarities. These LUs are designated by an alphabetical descriptive abbreviation. For instance, BG stands for Bedded Gravels and SSd for Silty Sand deposits (Fig. SI-1). Based on sedimentological criteria, each of these LUs was then subdivided into stratigraphic layers, which are designated by adding a sequential number from top to bottom. Four major stratigraphic layers were recognized in the SSd unit (Fig. SI-1), and these can be generally traced across the exposed profiles at the site despite localized grain-size variations and grading contacts (Fig. SI-2). Given the laminated nature of the deposits at Boker Tachtit, further subdivisions into individual depositional lenses and microfacies can be made within each stratigraphic unit.

It is within the SSd large-scale unit that individual archaeological horizons were differentiated. These horizons were distinguishable based on the presence of high densities of lithic artifacts interspersed by archaeologically sterile deposits. The identified horizons can be directly correlated with those studied by Marks (1) (Fig. SI-3). In terms of overall stratigraphic correlations, the previous descriptions by Goldberg (2) focused primarily in the area of Section A, that is, the easternmost sections of the site adjacent to a recent erosional gully. Unfortunately, these deposits that were exposed during the 1975 fieldwork, were subsequently excavated or not exposed during our recent excavations that focused primarily on the better preserved and unexcavated western sections of the site. Nevertheless, general correlations can be made between the two stratigraphic frameworks. Lithostratigraphic unit BG corresponds to layers 3-5, and the finer deposits associated with our SSd unit correlate to the 6-12 subdivisions in Goldberg (2). Subdivision SSd-3 in the current excavation corresponds to layer 9 in the previous excavations. It is interesting to note that SSd-3 stratigraphic layer presents one of the most significant lateral variations, with several coarser grain-sized channels illustrated in the profiles in Goldberg (2) and in our squares PP>OO 16>15 (Fig. SI-3). These deposits show localized relative higher-energy alluvial depositions and contrast with the overall finer, lower-energy sedimentation that

characterizes the SSd lithostratigraphic unit as a whole. Substantially higher depositional energy is again visible in association with the stratigraphically higher BG unit, which is composed of coarse pebbles and boulders. The contact between BG and SSd is a sharp stratigraphic unconformity, which involved considerable erosion of the uppermost layers of the SSd unit. This erosion was more substantial towards the west, where a considerable thickness of the deposits was lost and a direct stratigraphic contact between the BG and the lowermost subdivision, the SSd-4 layer, can be seen (Figure 2 in main text). This contrasts with the area of section D, where roughly 1m thick SSd deposits overly layer SSd-4. An outcome of this depositional shift is that some archaeological horizons are not equally preserved across the site. Detailed stratigraphic descriptions presented in figures SI-1, SI-2 and figure SI-3, show the lateral extension of each stratigraphic unit in several of the recently excavated profiles.

BG: up to ~ 300 cm thick. Bedded, varying from clast- to matrix supported pebbles and cobbles in a yellow to brownish yellow (10YR 7/8 and 10YR 6/8) loose silty sand matrix with thin lenses of coarse sands with relatively fewer gravels. Though varying both laterally (in terms of the size of the clasts) and vertically (in respect to sandier or more gravelly layers), on the whole the deposits show normal grading and an apparent inclination towards North. The gravelly fraction is composed of few angular flints and very frequent rounded to sub-rounded chalks and limestone, with a size mode around 20 cm in diameter, though dm-sized boulders are also present and tend to be more abundant towards NE.Lower limit sharply truncates the underlying SSd complex in an irregular, wavy unconformity, sometimes showing undercutting.

SSd-1: ~ 70 cm thick. Brown to very pale brown (2.5Y 8/2 and 10Y 7/4) fine silts, with occasional dispersed fine sands and with few discrete lenses of medium to coarser calcareous sand. Massive to weakly bedded. Few lenses richer in stones (typically ~3 cm in diameter) and very few larger (10 cm in diameter) angular stones. Small-scale bioturbation channeling and larger (up to 10 cm in diameter) krotovinas (filled with loose brownish yellow deposits). Clear lower limit.

SSd-2: ~25 cm thick. Dark yellowish brown (10YR 4/4) sandy clays containing abundant lithic artifacts, frequently scattered charcoal fragments and some localized reddened domains = archaeological horizon A (AH-A) and corresponds to archaeological layer 4 of Marks' excavations. Few large angular to sub-rounded stones. Laterally, AH-A associated sediments tend to be less clayey and with a whitish calcitic nature with pale brown clayey domains, commonly cemented. Centimeter-large gypsum crystals. Below, deposits are well-sorted white to very pale brown (10 YR 8/1 to 8/2) sands and silts, occasionally embedding discrete pebbly lenses (clasts size has a mode around 5 cm in diameter). Porosity is low, with exception of mm-thick vertical dissection cracks with large gypsum crystals. Some bioturbation is observed, namely small-scale biochanneling and small, ~2cm in diameter, krotovinas. Lowermostdeposits tend to be whitish calcareous mud bedded laminations, interspersed by slightly darker laminations, typically each lens being 3 to 5 cm thick. Clear to diffuse lower limit.

SSd-3: ~30 to 60 cm thick. Coarser deposits that vary significantly across the profiles, both in terms of grain size (rare boulders, coarser cobbles and silty sands) and thickness of individual lenses. Gravelly-rich lenses tend to be discontinuous, commonly pinching out laterally and interspersed by very pale brown (10 YR 7/4) coarse/medium sands and silts. Clasts are typically sub-angular to rounded chalks with very few flint nodules. Coarser and thicker accumulation of gravels and rare boulders is present in squares PP>OO 16/15 with sharp contact with the overlying and underlying sediments. In section D, deposits are matrix-supported small cobbles and pebbles size range and laterally discontinuous. Towards North (squares UU 21/22), several upward coarsing lenses with rounded to sub-angular pebbles (~10 to 5 cm in diameter) are observed. Lower limit is sharp, erosive.

SSd-4: ~20 cm thick. Towards South (in squares OO/NN 16/14 and MM 13/12), the deposits are light yellowish brown loamy silts (10 YR 6/4) with common dark brown dendritic Mn coatings. Common lithic artifacts and some charcoals, namely a 3 cm thick by at least 70 cm in length lens of brown sands and silts (10 YR 4/3) containing a relatively higher concentration of charcoal fragments in squares MM 13/12. Towards North, the deposits are very pale brown (YR 7/4) sandy silts with lenses of coarse sands and granules, showing similar dark brown dendritic coatings. Occasional lithic artifacts and very few (~3 cm) stones. Lower limit not reached.

Figure SI-1: Boker Tachtit stratigraphic descriptions. LU = Lithostratigraphi units; AH = Archaeological Horizons. Lines in black in the photograph show the contacts between the main stratigraphic layer subdivisions. Color designations are based on Munsell soil-color chart on dry bulk samples.

Figure SI-2 Photograph of current excavation areas showing the unconformable contact between the coarser BG unit above and the finer laminations of unit SSd below. Stratigraphic subdivisions are highlighted in several profiles, as well as the general location of the archaeological horizons. Note the channelized and coarse grain size composition of stratigraphic layer SSd-3 towards the right in the photograph and its lateral variation across the profiles. Scale is 50 cm, with 10 cm increments.

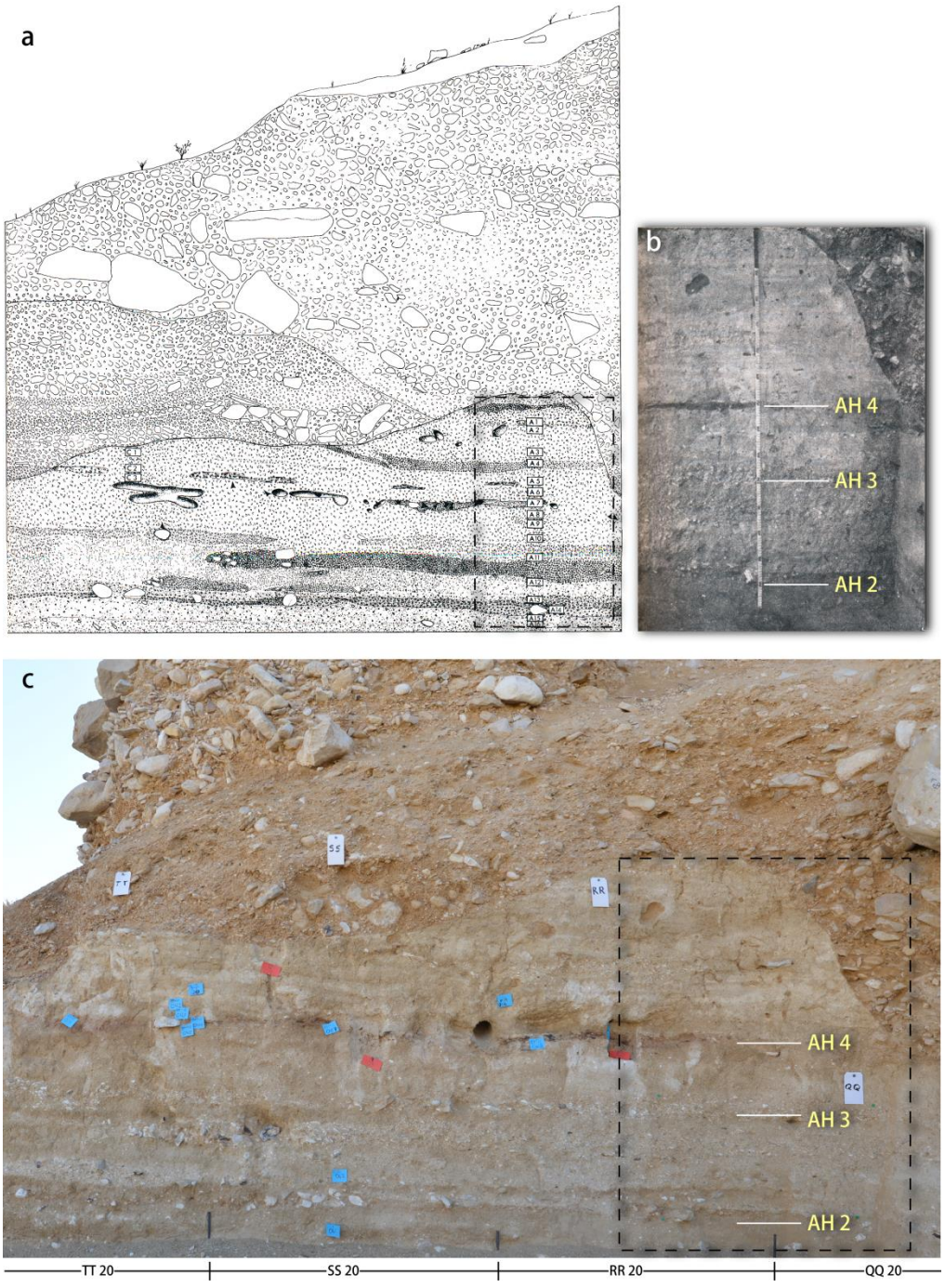

Figure SI-3. Boker Tachtit stratigraphic profile in the area of Marks' section D – current excavation squares TT-QQ20: **a**) modified profile drawing published in Marks (1983, p. 31), where the wavy sharp contact between the lower finer sediments (SSd unit) and the upper gravels (BG unit) is clear and easily identifiable. Note that the numbered boxes in the drawing represent sediment samples (see Marks, 1983) (1). The dashed square marks the area of the profile shown in (b) and in (c); **b**) modified photograph from Goldberg (1983, p. 45) (2), with the annotation of the archaeological horizons as mentioned in the

original figure caption; **c**) photograph of the current excavations showing the exposure of Section D, with the annotation of the area shown in (b) and (a), and the location of the archaeological horizons as defined from the previous excavations.

SI-2. The 2013-2015 excavation

The renewed excavations at Boker Tachtit were conducted in an area of ca. 15 m^2 along the edges of the previous excavations (Figs. SI-4; SI-5; SI-7). A new grid was established and aligned with the former grid set up by Marks (1). The field method included piece plotting of artifacts larger than 2 cm. All sediments were dry sieved using 2mm mesh. Charcoal samples for dating were handpicked and piece plotted. Two mechanical trenches were excavated from the lowermost part of Marks' excavation to a depth of ca. 2.5. m. The trenches produced no archaeological finds below, thus Marks's Level 1 is the earliest occurrence of occupation at Boker Tachtit.

Archaeological horizon A (AH-A) was identified in most of the sections (Figs. SI-5; SI-8). The association of this horizon with Level 4 from Marks's excavation is based on the uncovering of section D (Fig. SI-3) and matching the marked level in figure SI- 3A and the photograph in figure SI-3b. AH-A (or Marks's Level 4) was uncovered in three separate and discontinuous loci, covering a total area of 10 m^2 with a thickness of 40 cm (Fig. SI-5).

Notably, a small pit with charcoal fragments was identified in the eastern part of the excavated area (Fig. SI-6). Our field observations, that were later supported by radiocarbon dates, show this feature is intrusive and is likely to represent an animal burrow or a tree trunk.

Archaeological Horizon B (AH-B) was uncovered some 50 cm below AH-A in the western part of the site (Fig. SI-7). A total of 4 m^2 were excavated to a depth of ca. 30 cm. During the field work it was difficult to determine if this horizon should be associated with Level 2 or Level 1 from the old excavation. Post excavation examination suggested that this is Level 2 based on two independent observations. The first is a stratigraphic correlation with the section D from Marks' excavation where Level 2 is noted (Fig. SI-3). Cleaning the entire section enabled us to follow this level all the way around to the western part of the site (Fig. SI-8). The second evidence is conjoining pieces originating from neighboring excavated squares from the new excavations and the old excavations that unequivocally associated AH-B with Level 2 (Fig. SI-13).

Figure SI-4. A view to the east of the new excavation at Boker Tachtit.

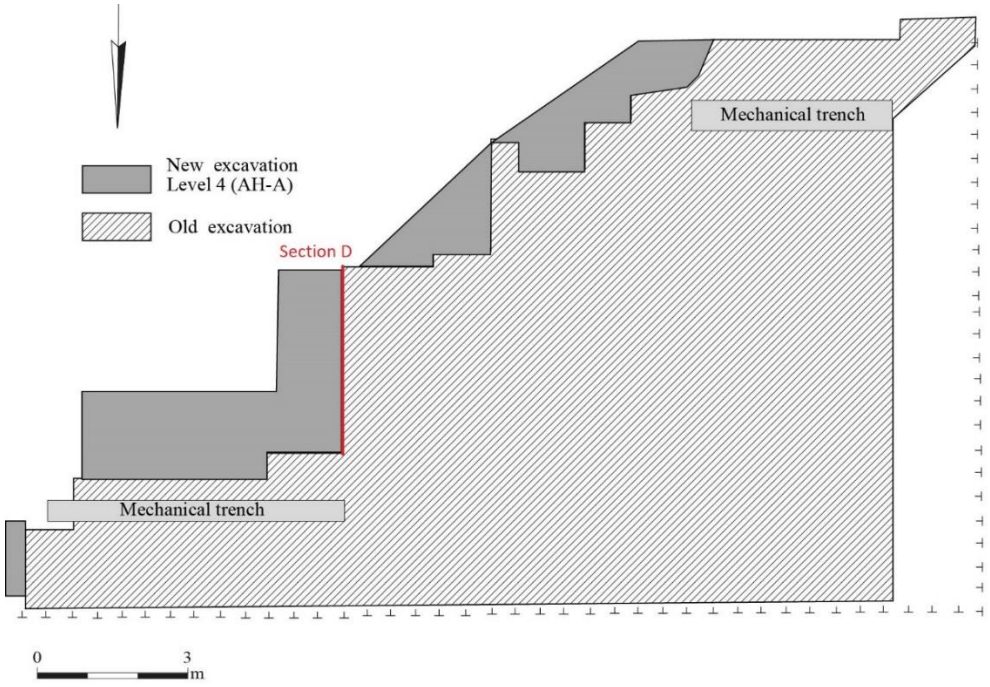

Figure SI-5. New excavation plan of AH-A at Boker Tachtit.

Figure SI-6. A pit with organic remains (encircled) that cut through AH-A.

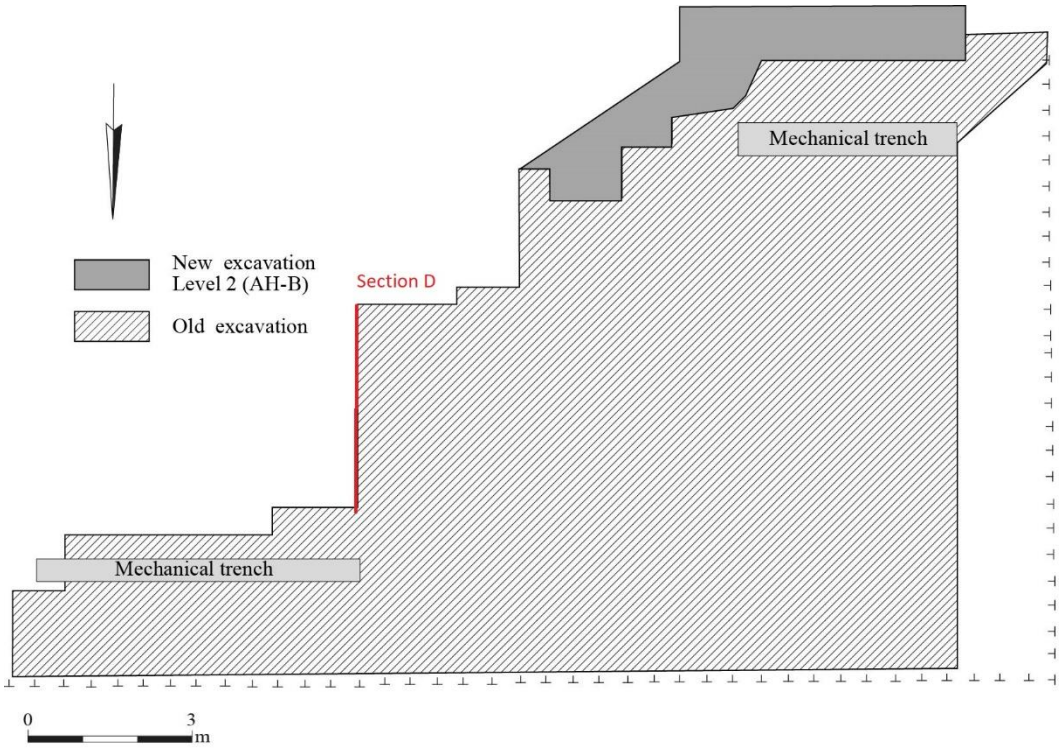

Figure SI-7. New excavation plan of AH-B at Boker Tachtit.

Figure SI-8. Exposures of AH-A and AH-B in the sections of the new excavation.

SI-3. Lithics

The excavated lithic assemblages consist of 2472 artifacts from AH-A and 3,666 artifacts from AH-B (Table SI-1), representing a higher artifact density for AH-B. The assemblage from AH-A is technologically characterized by the production of blades and elongated points following a unidirectional volumetric concept. The assemblage from AH-B is dominated by the production of elongated blades and points, that were knapped following both a surface exploitation concept and a volumetric concept from single and opposed platform cores.

	AH-A		AH-B	
Retouched tools	N	% within category	N	% within category
Typical end-scraper	9	17.6		
Typical burin	3	5.9	8	40.0
Typical borer	1	2.0	1	5.0
Truncated blade and flake	2	3.9	1	5.0

Notch	7	13.7	1	5.0
Multiple tool (burin on endscraper)			1	5.0
Retouched flakes	9	17.6	2	10.0
Retouched blades	3	5.9		
Retouched point	1	2.0	1	5.0
Emireh point			1	5.0
Triangular elongated points (no retouch)	16	31.4	4	20.0
Total	**51**	**100.0**	**20**	**100.0**
Core trimming elements (CTE)				
Ridge blade	1	1.8	40	34.2
Core tablet	6	10.9	8	6.8
Core trimming element	46	83.6	62	53.0
Burin spall	2	3.6	7	6.0
Total	**55**	**100.0**	**117**	**100.0**
Debitage				
Cores	9	1.6	21	2.5
Flakes	272	47.2	504	60.7
Blades	173	30.0	175	21.1
Bladelets	22	3.8	16	1.9
Flakes/blades with signs of use	3	0.5	35	4.2
Flakes/blades with isolated removals	3	0.5	4	0.5
fragments	94	16.3	75	9.0
Total	**576**	**100.0**	**830**	**100.0**
Debris				
Chunks	31		15	
Chips (artifacts <20mm)	1759		2684	
Total Assemblage	**2472**		**3666**	

Table SI-1. Boker Tachtit lithic assemblages by level.

Much of the knapping took place on site as evidenced by the high fraction of artifacts <20mm, and the refitting of artifacts in both levels. Micro-debitage analysis of sediments from section D showed a high concentration in AH-A (3), which is evidence for flint knapping activity.

Abundant flint outcrops in the Eocene limestone and chalk formations around the site can be found at distances ranging from 500m to 1km from the site. Wadi Zin drains a wider range of flint bearing geological formations, evident in the flint nodule variability found

in the dry river bed only 200m away from the site. The variability of flint nodules found at the site resembles that of Wadi Zin suggesting that the inhabitants of the site most probably selected raw material for working from Wadi Zin (4).

The lithic assemblage from AH-A is dominated by a single platform reduction sequence for the production of blades and points following the volumetric concept (Fig. SI-9). None of the cores reflect preferential point removal; rather they reflect a serial removal of blanks with the points amongst them. Ridge blades are almost absent, while core tablets and diagnostic blade technology core trimming elements are evident (Fig. SI-10:1-4). Thick triangular points resemble Levallois points but tend to be thicker (Fig. SI-10:6-10). Points and end scrapers made on a blade blank are the dominant tool types (Table SI-1).

The lithic assemblage from AH-B displays a higher level of technological variability when compared to AH-A. Three different reduction sequences are present following two different concepts; the volumetric and the surficial concepts. The surficial exploitation approach (Fig. SI-11:1,3) draws from the Levallois technology, but does not belong to the Levallois technological concept as it does not comply with the Levallois definition (5,6). None of the cores from the new assemblage resemble a Levallois point core, nor do any of the cores reflect a removal of a point as the final end product. Cores associated with the volumetric concept (Fig. SI-11:2, 4), in their final form reflect the exploitation of the wide face of the core with unidirectional and bidirectional removals. Both these reduction sequences are associated with an intensive use of ridge blades (Fig. SI-12:1,2,4,5) for core shaping and maintenance. Core tablets are few and atypical (Fig. SI-12:3). The third group of cores (Fig. SI-11:5-6) are conceptually cores on flakes (7), reflecting the exploitation of thick flakes as cores.

The dominant tool type is the burin (Fig. SI-12:13-15). The only endscraper (Fig.SI-12:13) in this assemblage is the one with the burin blow made on a flake blank. Un-faceted triangular points (Fig.SI-12:7-9) have similar characteristics to those from AH-A, with thick cross sections, and three with facetted striking platforms. Two retouched points were found; one is an Emireh point with basal thinning (Fig.SI-12:12), the other is a short wide point with retouch around the basal part of the point (Fig. SI-12:11).

Refitting of artifacts was possible in both archaeological horizons. Conjoining of artifacts was also possible between AH-B and Marks' Level 2, which is housed in the National Treasures collections of the Israel Antiquities Authority (Fig. SI-13).

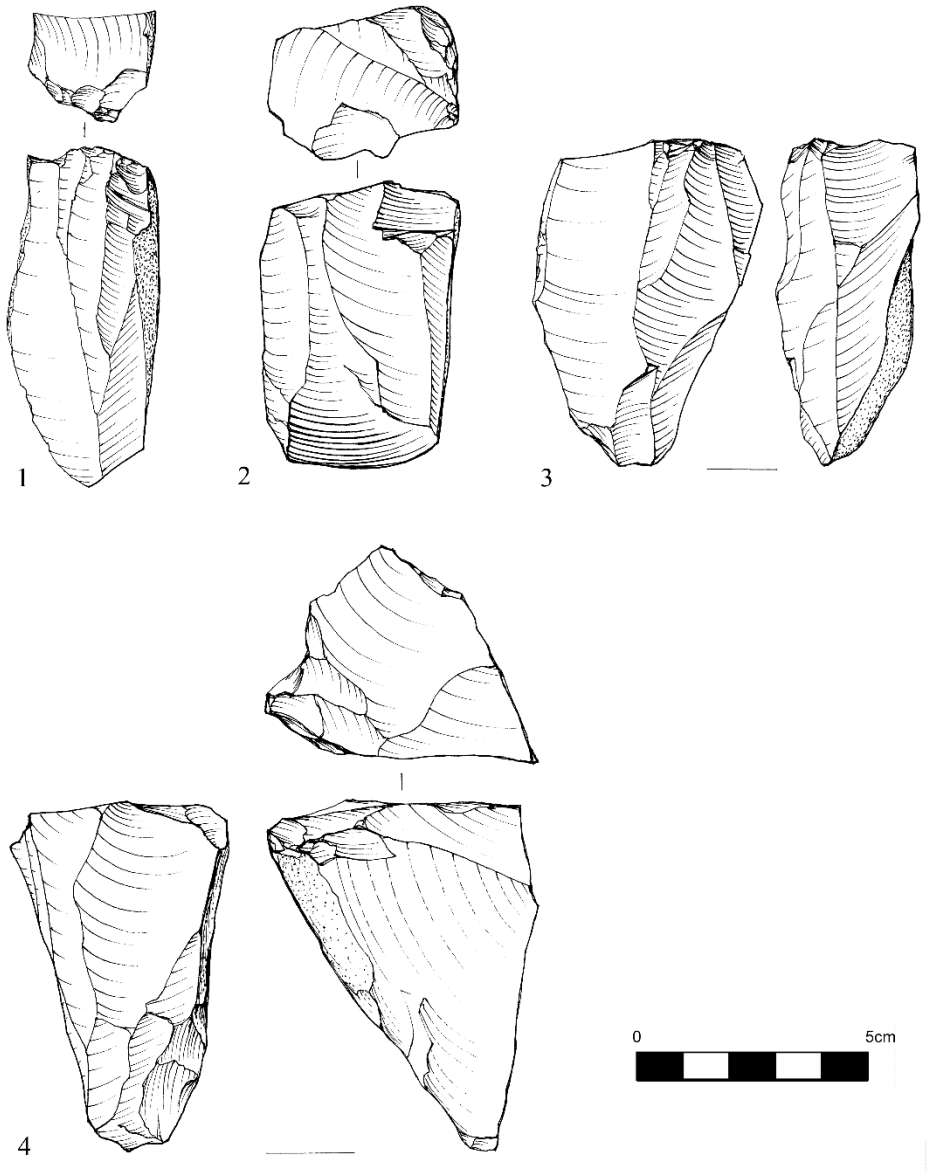

Fig. SI-9. Cores AH-A. Volumetric Single platform cores for blades. 3 and 4 have basal corrections.

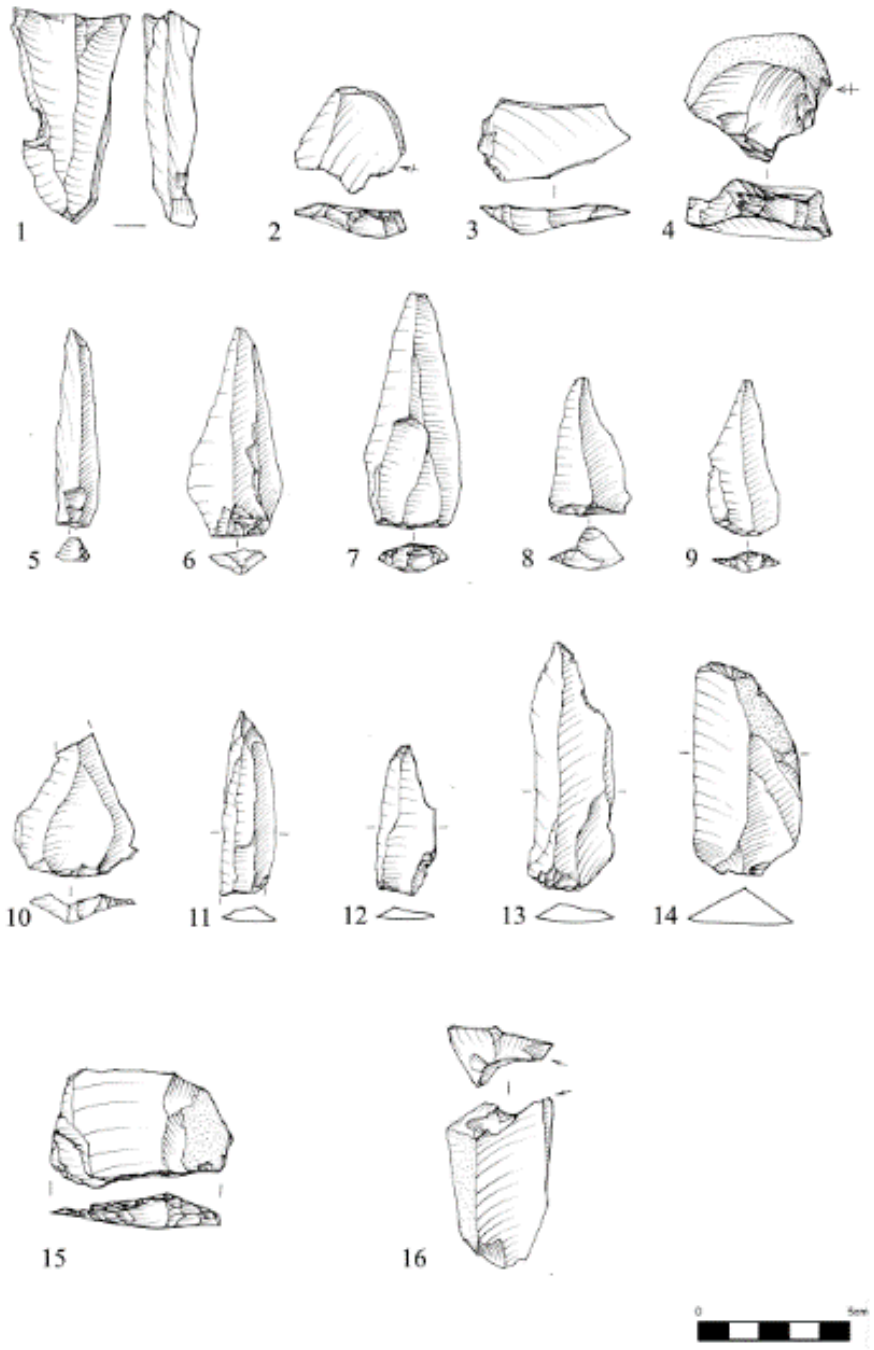

Fig. SI-10. CTE and tools AH-A. 1. CTE from blade core, 2-4. Core tables, 5. Blade, 6-7. Elongated points, 8-10. Triangular flakes, 11-12. Retouched points, 13. Notch on blade, 14. End scraper, 15. Truncation on proximal end, 16. Burin

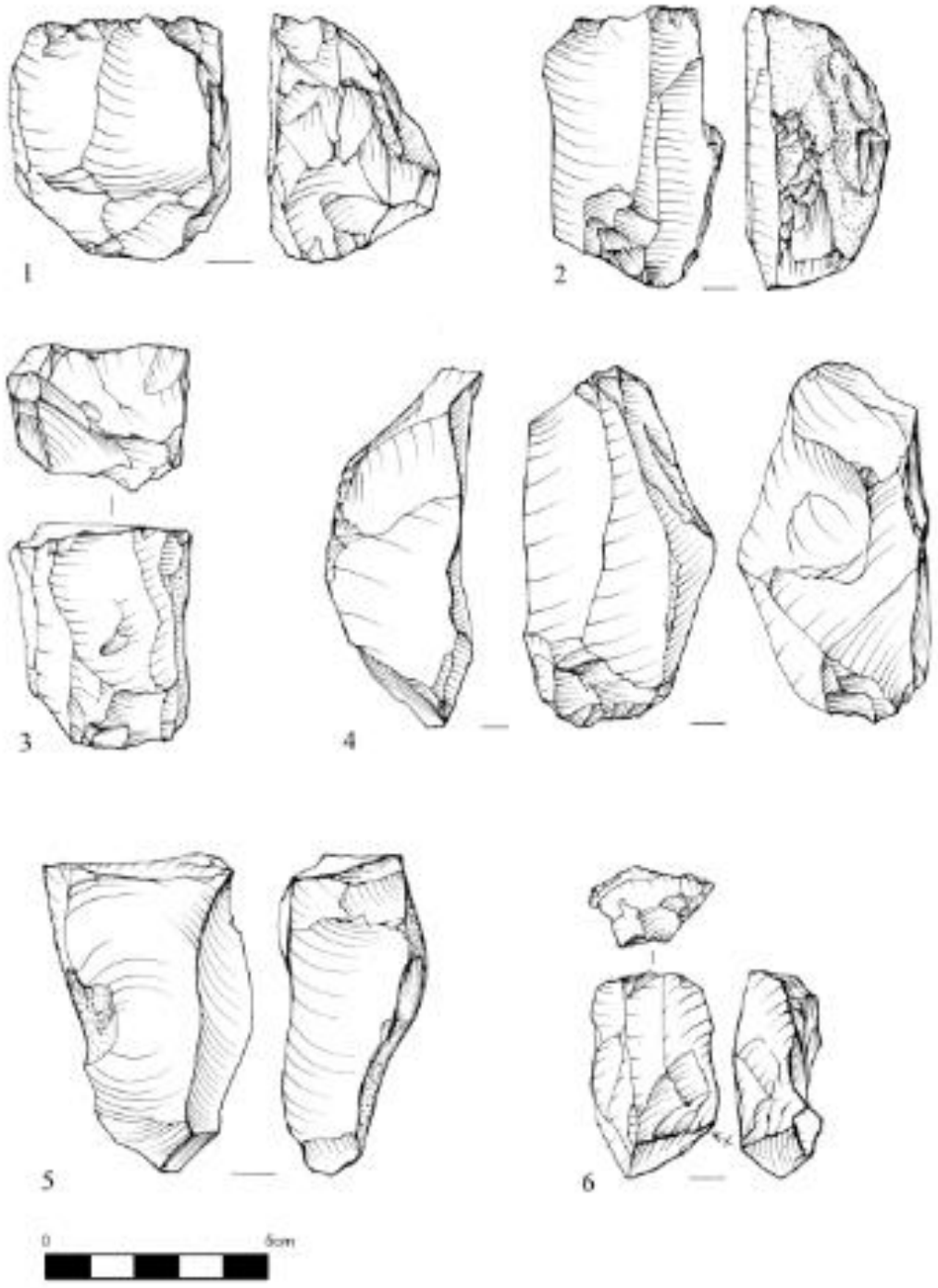

Fig. SI-11. Cores AH-B. 1,3. Surficial single platform cores, 2, 4 Bidirectional cores, 5-6. Cores on flakes

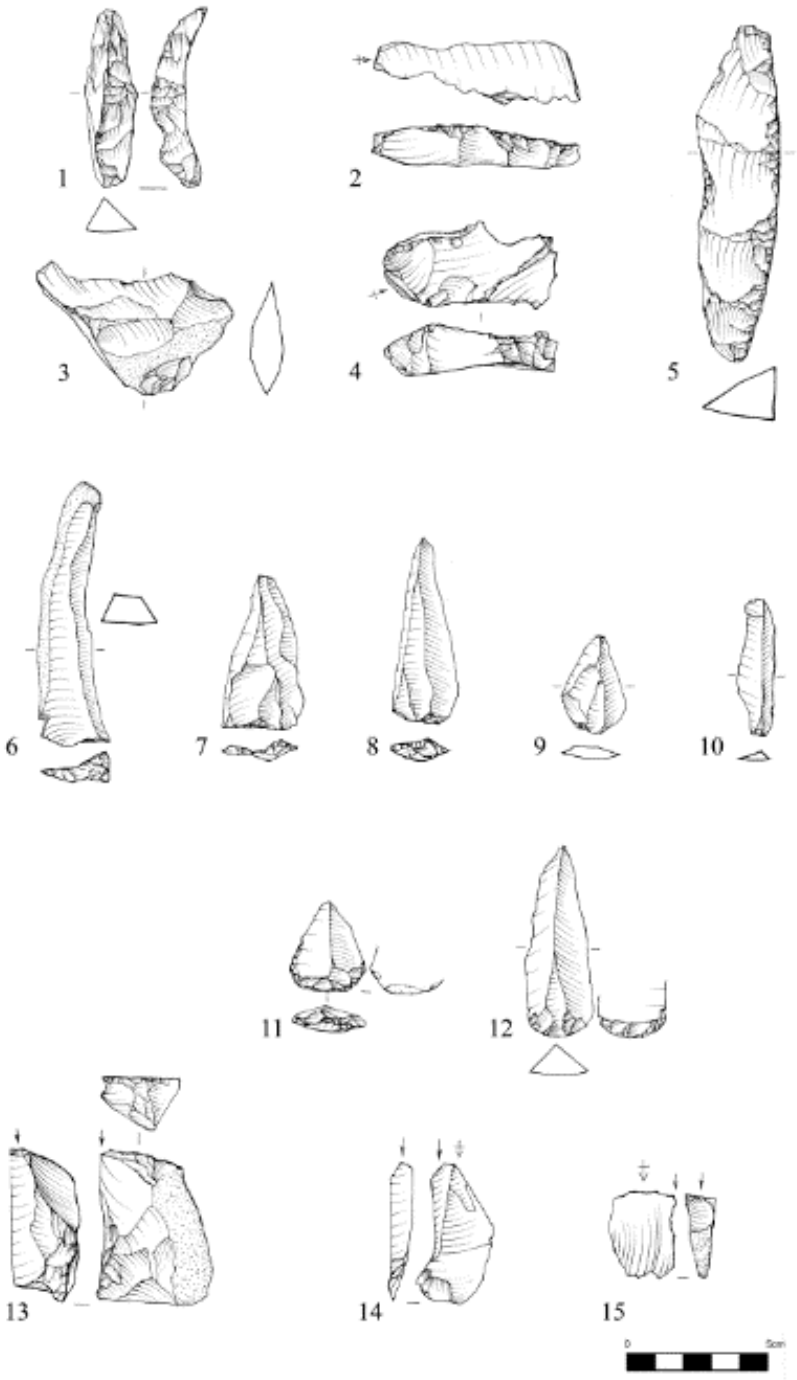

Fig. SI-12. CTE and tools AH-B. 1. Ridge blade (Double crested), 2, 5. Ridge blades (Single crested), 3. CTE, 4. Core tablet, 6,10. Blades, 7,8. Elongated points, 9. Flake, 11. Broad point with basal retouch, 12. Emireh point. 13. Burin on truncation, 14. Dihedral burin, 15. Burin on lateral edge.

Fig. SI-13. Conjoined ridge blade. Proximal part obtained from AH-B and the distal part from Marks level 2.

SI-4. Radiocarbon

The chronology of Boker Tachtit is based on dates of charcoals prepared by the ABA (Acid-Base-Acid) pretreatment. Charcoal samples were characterized and prepared for radiocarbon dating based on tailor-made procedures at the DANGOOR Research Accelerator Mass Spectrometry (D-REAMS) Laboratory (4,5,6). Before and after pretreatment, samples were analyzed by FTIR spectrometry to determine the purity of the material. Generally, 30-100mg of each charcoal sample was cleaned of sediment under a microscope with a scalpel and homogenized by crushing in an agate mortar and pestle. Samples were then treated using the ABA procedure: (a) acid treatment in 1 M HCl for 30 min, followed by rinsing with Nanopure water until the pH reached 6, (b) base treatment of 0.1 M NaOH for 15 min, followed by rinsing until the pH reached 6, and (c) acid treatment in 1 M HCl for 1 hour in a water bath of 80°C, followed by rinsing until the pH reached 6. The NaOH step was sometimes applied more than once if the color of the solution was still dark, indicating the presence of large amounts of humic substances. Samples were dried overnight at ~60°C, combusted to CO_2 with ~200 mg of CuO at 900°C in vacuum, and then reduced to graphite in the presence of hydrogen at 680 °C. All samples from Boker Tachtit were very small in size which was not enough to test ABA vs ABOx procedure. However, such a comparison has been rigorously carried out in two other sites, Kebara and Manot caves (5, 13). The conclusions from these studies were that the ABOX treatment resulted in more erratic results, and mostly younger or similar dates to the ABA. This is presumably due to a significant loss of wood charcoal, thus increasing the contribution of carbon associated with the clays which were detected with FTIR. All samples were measured by AMS at the D-REAMS Laboratory (6).

Four samples were treated with HF (hydrofluoric acid) due to the presence of large amounts of clay after pre-treatment. Lack of removal of the clay was proven to introduce

contamination as the radiocarbon age of these samples was systematically much younger than the expected age. The complete list of samples analyzed for radiocarbon, including those analyzed for radiocarbon but rejected, is given in **Table SI-3**. Calibration of radiocarbon dates is based on the new calibration curve (7) for terrestrial samples.

Background level for the corrections of the samples from the site have been determined during the analysis of the samples. Table SI-2 shows the background data.
The most relevant columns are the pMC columns for the general background and for the 3 oldest samples (uncorrected for the background) from the project (last two columns).

Method	Size [mg]	pMC	pMC ±1σ	No. of BGDs	Sample RTD	Sample pMC (no BGD correction)
ABA	1	0.268	0.014	13	8155.1	0.518±0.016
	0.5	0.245	0.016	2	8148	0.820±0.027
	0.3	0.241	0.014	1	8150	1.069±0.034
	All	0.264	0.015	16		
ABA MP/UP	1	0.244	0.018	5	7740.2	0.597±0.023
ABAHF MP/UP	1	0.624	0.032	2	7147	1.503±0.034
WHFBA	1	0.381	0.016	1	7321	1.168±0.028
	0.4	0.694	0.046	1	7322.2	1.111±0.044
WHFBA MP/UP	1	0.212	0.017	3	7733	0.768±0.038

Table SI-2. Background results in pMC related to the samples measured in this study.

This clearly shows that pMC values of the samples are significantly higher than the background values. According to Stuiver and Polach (1977) (8) a finite radiocarbon age is given to a sample with a pMC value larger than its 2σ. As can be seen in Table SI-2, this is the case for all our samples in Boker Tachtit. In addition, no sample yielded a lower pMC value than its corresponding background. Therefore, all the samples in this study were calculated as any standard radiocarbon sample, by simple background subtraction.

TABLE SI-3 Radiocarbon results

Level	Locus	Archaeological Context	RTD #	Basket	Elevation above datum (m)	Botanical Identification	Pre-treatment		Libby Age ± 1σ year BP	Calibrated range 68.2% BP (7)	Note
							Eff. %	C %			
AH-A	205	Section D. Flint artifacts horizon. Mainly large flakes and blades, some bearing cortex. Embedded in light compacted sediment.	7736.1 7736.2 7736.3	2411	50.46 (50.51- 50.67	*Pistacia atlantica*	29.2	68.6	42059 ± 682 42365 ± 711 41028 ± 638 **Average** **41828 ± 391**	X2-Test: df=2 T=2.2(5% 6.0) **44904 - 44369**	ABA
	217	The lower part of AH-A. Several large pebbles and hammerstones.	7739.1 7739.2	2583	50.34- 50.55	*Pistacia atlantica*	29.6	61.5	43331 ± 795 44672 ± 941 **43972 ± 610**	X2-Test: df=1 T=1.2(5% 3.8) **46934 - 45665**	ABA
			7741.1 7741.2	2604	50.34- 50.55	*Pistacia atlantica*	22.9	65.3	44267 ± 893 44361 ± 898 **Average** **44314 ± 634**	X2-Test: df=1 T=0.0(5% 3.8) **47316 - 45966**	ABA
AH-B	225	Upper part of AH-B in SW area. Several small charcoal fragments and small lithic artifacts.	8163	3038 3039 3046 3049	49.86- 50.01	*Juniperus* cf. *phoenicea*	21.3	58.4	41713 ± 419	44863 - 44280	ABA
			8146	3047	49.86- 50.01	*Juniperus* cf. *phoenicea*	10.4	56.0	43331 ± 493	46110 - 45215	ABA
	227	Upper AH-B with lithic artifacts of medium size debitage (mainly chips, large amount). Small charcoal fragments.	8158.1	3118 GC	49.85- 49.97	*Juniperus* cf. *phoenicea*	37.5	57.5	41299 ± 390	44631 - 43971	ABA
			8156	3135	49.85- 49.97	*Tamarix* sp.	34.8	48.0	41907 ± 506	45070 - 44349	ABA
			8164	3073 3076 3081 3094 3098 3099 3101	49.85- 49.97	*Juniperus* cf. *phoenicea*	20.9	47.6	43461 ± 503	46254 - 45279	ABA
			8154	3091 GC	49.93- 49.82GC 49.85- 49.97	*Juniperus* cf. *phoenicea*	22.7	48.0	44627 ± 737	47687 - 46139	ABA

Level	Locus	Archaeological Context	RTD #	Basket	Elevation above datum (m)	Botanical Identification	Pre-treatment		Libby Age ± 1σ year BP	Calibrated range 68.2% BP (7)	Note
							Eff. %	C %			
			8147.1 8147.2	3071	49.85-49.97	cf. *Hammada scoparia*	13.6	56.1	44896 ± 591 45127 ± 747 **Average 44987 ± 464**	**X2-Test: df=1 T=0.1(5% 3.8) 47905 - 46762**	ABA
			8165	3077 3080 3109 3115 3116 3129 3334	49.85-49.97	*Tamarix* sp.	27.1	45.0	45293 ± 613	48267 - 46876	ABA
			8155.1 8155.2	3137	49.85-49.97	*Juniperus* cf. *phoenicea*	25.6	53.0	47274 ± 747 47053 ± 1155 **Average 47211 ± 628**	X2-Test: df=1 T=0.0(5% 3.8) **50640 - 48633**	ABA
AH-B	228	Lower AH-B. Highly concentrated surface, with large lithic artifacts including cores and hammerstones. Charcoals fragments	8161	3140	49,9-49,81 top and bottom GC	*Tamarix* sp.	15.7	44.0	41310 ± 396	44640 - 43974	ABA
			8160.1	3140	49,9-49,81 top and bottom GC	*Juniperus* cf. *phoenicea*	37.4	60.2	43266 ± 482	46050 - 45195	ABA
			8149	3142	49.84	*Juniperus* cf. *phoenicea*	11.3	57.4	44017 ± 532	46910 - 45790	ABA
			8162.1	3140	49,9-49,81 top and bottom	cf. *Hammada scoparia*	33.6	59.3	47039 ± 744	50574 - 48387	ABA
	218	Light clay, sterile. Below lithic artifacts of Lower AH-B	7740.1 7740.2	2584 2584	49.96-50.05	*Juniperus* cf. *phoenicea*	34.0	62.9	45840 ± 1101 46362 ± 1185 **Average 46095 ± 808)**	X2-Test: df=1 T=0.1(5% 3.8) **49648 - 47581**	ABA

Level	Locus	Archaeological Context	RTD #	Basket	Elevation above datum (m)	Botanical Identification	Pre-treatment		Libby Age ± 1σ year BP	Calibrated range 68.2% BP (7)	Note
							Eff. %	C %			
		HF Pre-treatment									
AH-A	217	The lower part of AH-A. Several large pebbles and hammerstones.	7738.1 7738.2	2570	50.34-50.55	*Juniperus* cf. *phoenicea*	9.53	50.0	38804 ± 242 39552 ± 269 **Average 39178 ± 529**	**42963 - 42455**	WHFBA
AH-B	203	Concentration of lithic artifacts. Relatively large artifacts.	7731	2045	49.99-50.08	*Juniperus* cf. *phoenicea*	7.15	41.5	39643 ± 503	43293 - 42588	WHFBA
	206	Flint exposure and large charcoal samples. Relatively high flint density. **14303 39771**	7735.1 7735.2	2405	49.86-50.01	*Juniperus* cf. *phoenicea*	22.1	41.0	39169 ± 263 39130 ± 270 **Average 39150 ± 189**	X2-Test: df=1 T=0.0(5% 3.8) **42791 - 42581**	WHFBA
		No FTIR spectrum									
AH-A	214	Cuts into L205. Unclear whether it represents bioturbation or anthropogenic activity. A thin layer of charcoal is evident throughout the feature. One flint artifact was found in its sediment.	7734	2340	50.39-50.56	*Tamarix* sp. branch <6mm	4.36	57.0	31118 ± 315	35941 - 35229	ABA WHFBA
AH-A	217	The lower part of AH-A surface. Several large pebbles and hammerstones.	7742	2617	50.34-50.55	*Pistacia atlantica*	6.53	61.0	29533 ± 139	34297 - 33981	WHFBA
AH-B	202	Compacted silty sediment containing lithic artifacts. Probably corresponding to the upper part Level 2.	7732	2069	50.05-50.15	*Juniperus* cf. *phoenicea*	6.67	51.0	36523 ± 482	41865 - 41175	ABA
AH-B	206	Flint exposure and large charcoal samples. Relatively high flint density (compared to L202-203)	7733	2328	50.08-50.11	*Juniperus* cf. *phoenicea*	7.5	69.7	41710 ± 593	45056 - 44129	WHFBA

Level	Locus	Archaeological Context	RTD #	Basket	Elevation above datum (m)	Botanical Identification	Pre-treatment		Libby Age ± 1σ year BP	Calibrated range 68.2% BP (7)	Note
							Eff. %	C %			
AH-B	228	Lower Level 2. Highly concentrated surface composed of large lithic artifacts including cores and hammerstones.	8159	3140 GC	49.9-49.81 (49.80-49.85)	*Pistacia atlantica*	28.1	70.5	40941 ± 484	44380 - 43408	ABA
		Poor context									
AH-B	101	Very few lithic artifacts. Sediment contains gypsum. Maybe lowermost Level 2 exposure (large charcoal)	7322.1 7322.2	1072	49.64-49.72	*Tamarix* sp.	8.18	72.5	37632 ± 255 38192 ± 424 **Average 37792 ± 219**	X2-Test: df=1 T=1.3(5% 3.8) **42301 - 42109**	ABA FTIR good charcoal
AH-A	103	Compacted silty sediment. Probably base of a channel that cut Level 4.	7321	1049	50.4	*Tamarix* sp. (30frgs)	5.25	54.0	39847 ± 299	43224 - 42799	ABA High humic presence. FTIR good charcoal
		Poor C %									
AH-A	108	Continuation of a surface composed of flint artifacts that was exposed in section D and in L104. Dense accumulation of flint artifacts embedded in brown clay sediment.	7320	1548	50.54-50.72	*Tamarix* cf. *aphylla*	1.76	12.0	16316 ± 958		ABA FTIR clay.
			7319	1446	50.54-50.72	*Tamarix* cf. *aphylla*	8.00	16.2	19018 ± 738		FTIR clay.
AH-B	102	Few lithic artifacts, incorporated in a calcium carbonate matrix.	7146	1021 (2)	49.91-49.95	*Juniperus* cf. *phoenicea*	1.84	22.0	32808 ± 364	37742 - 36573	FTIR high clay
			7147	1013	49.91-49.95	*Tamarix* sp.	23.0	32.0	35160 ± 221	40586 - 40028	FTIR good charcoal.

Level	Locus	Archaeological Context	RTD #	Basket	Elevation above datum (m)	Botanical Identification	Pre-treatment		Libby Age ± 1σ year BP	Calibrated range 68.2% BP (7)	Note
							Eff. %	C %			
	224	Cleaning L216 from the previous season. Few lithic and charcoal pieces.	8153	3043	49.91-49.92	*Juniperus cf. phoenicea*	21.6	39.4	36119 ± 286	41418 - 40929	ABA
	227	Upper Level 2 with lithic artifacts of medium size debitage (mainly chips, large amount). Small charcoal fragments.	8148	3107	49.81 (49.85-49.97)	*cf. Hammada scoparia*	12.7	24.0	41318 ± 464	44704 - 43888	ABA
	228	Lower Level 2. Highly concentrated surface composed of large lithic artifacts including cores and hammerstones.	8150	3191	(49.80-49.85)	*Juniperus cf. phoenicea*	11.0	32.0	38523 ± 387	42610 - 42300	ABA
			8157	323 (21/4/15) or 3140	49.80-49.85	*Tamarix sp.*	40.9	38.4	41771 ± 396	44875 - 44333	ABA FTIR clay

Table SI-3: Charcoal samples analysed for radiocarbon dating from the different levels. Level, Locus, archaeological context, Laboratory number (RTD #), basket number, relative elevation, botanical identification, chemical recovery (efficiency %), carbon percentage after pre-treatment (Carbon %), Libby age and comments on pre-treatment procedures. Note ABA = Acid-Base-Acid treatment, WHFBA = Water-Hydrofluoric Acid-Base-Acid treatment, GC general charcoal indicates that several charcoal fragments from the same locus and the same species were combined for the analysis, FTIR (Fourier Transform Infrared analysis): the main finding is stated if relevant.

TABLE SI-4. Radiocarbon results from the Levant

Lab code	Layer	material	Pre-treat.	Lithic industry	^{14}C yr uncal BP	±1σ	±1σ Calibrated range year BP based on (7, 14)	
Üçağızlı (9)								
AA-68965	I	charcoal	ABOX	IUP	39817	599	43818	42670
AA-68962	I	charcoal	ABOX	IUP	36915	335	41996	41507
AA-68963	I	charcoal	ABOX	IUP	33874	271	39395	38517
AA-52052	I	charcoal	ABA	IUP	40200	1300	44417	42680
AA-52054	I	charcoal	ABA	IUP	39700	1600	44475	42335
AA-52051	I	charcoal	ABA	IUP	39200	1300	43939	42258
AA-52055	I	charcoal	ABA	IUP	35100	1400	41782	39019
AA-37625	H-H3	charcoal	ABA	IUP	41400	1100	45072	43260
AA-27994	H-H3	charcoal	ABA	IUP	39400	1200	43921	42369
AA-27995	H-H3	charcoal	ABA	IUP	38900	1100	43766	42111
AA-35261	H-H3	charcoal	ABA	IUP	35670	730	41372	40055
AA-52050	H-H3	charcoal	ABA	IUP	35500	1200	41657	39573
AA-37626	G	charcoal	ABA	IUP	39100	1500	44132	42144
AA-37624	Fb-c	charcoal	ABA	IUP	35020	740	40907	39503
AA-35260	Fb-c	charcoal	ABA	IUP	34000	690	39790	37835
AA-42321	C	charcoal	ABA	Ahmarian	29060	330	34035	33165
AA-42317	B1-3	charcoal	ABA	Ahmarian	34580	620	40530	39185
AA-38021	B1-3	shell	ABA	Ahmarian	32670	760	**37208**	**35439**
AA-42320	B1-3	charcoal	ABA	Ahmarian	31900	450	36768	35768
AA-38203	B	shell	ABA	Ahmarian	29130	380	**33076**	**32012**
***Üçağızlı* (10)**								
OxA-20628	H3	shell	CarDS	IUP	36320	270	40660	40114
OxA-19760	H	shell	CarDS	IUP	34050	170	38413	37737
OxA-19759	G	shell	CarDS	IUP	34540	180	39071	38573
OxA-X-2318-50	Fc	shell	CarDS	IUP	34300	800	39244	37381
OxA-19758	F	shell	CarDS	IUP	34080	180	38478	37773
OxA-21116	B1-B3	shell	CarDS	Ahmarian	35240	260	39664	39200
OxA-X-2338-55	B	shell	CarDS	Ahmarian	36270	240	40596	40091
Ksâr 'Akil (11)								
OxA-25656	XXVIIIA	shell	CarDS	MP	39530	330	**42507**	**42191**

OxA-20491	XXVIII	shell	CarDS	MP	39310	330	**42410**	**42102**
Combine OxA-20489/ OxA-20490	XXIII	shell	CarDS	Phase 1- IUP	37707	207	**41605**	**41245**
OxA-20489					36790	270		
OxA-20490					37430	320		
OxA-22667	XXII	shell	CarDS	Phase 1- IUP	34320	190	**38874**	**38228**
OxA-20880	XXII	shell	CarDS	Phase 1- IUP	34940	200	**39394**	**39007**
OxA-25655	XXII	shell	CarDS	Phase 1- IUP	30890	160	**34647**	**34314**
OxA-20025	XXI	shell	CarDS	Phase 1- IUP	36390	210	**40688**	**40240**
OxA-20879	XX	shell	CarDS	Phase 2- Ahmarian	35010	240	**39479**	**39034**
OxA-X-2361-14	XIX	shell	CarDS	Phase 2- Ahmarian	32960	160	**36799**	**36376**
OxA-22664	XIX	shell	CarDS	Phase 2- Ahmarian	35510	240	**39885**	**39410**
OxA-20488	XVIII	shell	CarDS	Phase 2- Ahmarian	34230	210	**38781**	**38034**
OxA-25653	XVIII	shell	CarDS	Phase 2- Ahmarian	34830	240	**39347**	**38849**
OxA-X-2338-8	XVIII	shell	CarDS	Phase 2- Ahmarian	33760	210	**38020**	**37282**
OxA-20486	XVII	shell	CarDS	Phase 2- Ahmarian	35780	240	**40157**	**39640**
OxA-25652	XVII	shell	CarDS	Phase 2- Ahmarian	33300	230	**37326**	**36694**
OxA-20487	XVII	shell	CarDS	Phase 2- Ahmarian	33930	220	**38293**	**37526**
OxA-22269	XVII	shell	CarDS	Phase 2- Ahmarian	35390	250	**39782**	**39314**
OxA-20877	XVII	shell	CarDS	Phase 2- Ahmarian	36270	240	**40596**	**40091**
OxA-X-2342-57	XVII	shell	CarDS	Phase 2- Ahmarian	28130	110	**31442**	**31163**
OxA-22665	XVI	shell	CarDS	Phase 2- Ahmarian	36040	240	**40398**	**39886**
Ksâr ʻAkil (12)								
GrA-53000	XXII	shell	HCl, H_3PO_4	Phase 1- IUP	40550	350/310	**43079**	**42617**
GrA-57597	XX	shell	HCl, H_3PO_4	Phase 2- Ahmarian	40040	340/300	**42759**	**42401**

GrA-53004	XIX	shell	HCl, H_3PO_4	Phase 2-Ahmarian	39390	330/290	**42445**	**42134**
GrA-57542	XVIII	shell	HCl, H_3PO_4	Phase 2-Ahmarian	36290	240/220	**40615**	**40111**
GrA-57603	XVII	shell	HCl, H_3PO_4	Phase 2-Ahmarian	38260	260/240	**41955**	**41599**
GrA-57602	XVII	shell	HCl, H_3PO_4	Phase 2-Ahmarian	36730	240/220	**40950**	**40526**
GrA-54846	XVII	shell	HCl, H_3PO_4	Phase 2-Ahmarian	39850	340/310	**42664**	**42321**
GrA-53001	XVII	shell	HCl, H_3PO_4	Phase 2-Ahmarian	34090	220/200	**38532**	**37739**
GrA-57599	XVI	shell	HCl, H_3PO_4	Phase 2-Ahmarian	39890	310/280	**42669**	**42348**
GrA-57598	XVI	shell	HCl, H_3PO_4	Phase 2-Ahmarian	37320	270/240	**41369**	**40940**
GrA-57544	XVI	shell	HCl, H_3PO_4	Phase 2-Ahmarian	35960	230/210	**40322**	**39820**
GrA-54847	XVI	shell	HCl, $_3PO_4$	Phase 2-Ahmarian	39910	370/320	**42708**	**42335**
Manot Cave (13)								
RTD7115	Level 7 J65	charcoal	ABA	Ahmarian	42210	390	45156	44566
RTD7196	Level 7 J65cd	charcoal	ABA	3827	41100	450	44519	43437
Kebara Cave (5)								
RTO-5801-1	V	charcoal	ABA	Mousterian	51500	1200	52833	50358
RTO-5800-1	V	charcoal	ABA	Mousterian	49600	1000	54751	52127
RTO-5798-1			ABA	Mousterian	46250	640	49552	47903
RTO-5682-1	V	charcoal	ABA	Mousterian	45200	700	48302	46741
RTO-5799-1	IV	charcoal	ABA	Early Ahmarian	36110	330	41453	40881
RTO-5681-1	IV	charcoal	ABA	Early Ahmarian	43600	600	46603	45393
RTO-5680-1			ABA	Early Ahmarian	41650	450	44856	44209
RTO-5589	IIIb	charcoal	ABA	Early Ahmarian	42850	550	45789	44892
RTO-5590			ABA	Early Ahmarian	42600	500	45522	44730

Combine RTO-5679-1 and 5679-2	IIIb	charcoal	ABA	Early Ahmarian	40550	283	43949	43269
RTO-5679-1					40500	400		
RTO-5679-2					40600	400		
Far'ah II (14)								
RTD 9448*	B1068, C-1	charcoal	ABA	LMP	47507	735	51356	48930
RTD 9449*	B1082, C-5	charcoal	ABA	LMP	52721	1323	out of range	
RTD 9544	L2d B1090	charcoal	ABA	LMP	44688	666	47679	46221
RTD 9545	L2d B1090	charcoal	ABA	LMP	44825	820	47940	46218
Abu Noshra I (15)								
B-12125		charcoal		EUP	**>30440**			
SMU-2254		charcoal		EUP	35824	1090	41790	40010
SMU-2007		charcoal		EUP	35805	1520	42068	39589
SMU-1824		charcoal		EUP	31330	2880	40387	33174
B 13898		charcoal		EUP	29580	1610	35738	31965
B 13897		charcoal		EUP	25950	360	30737	29965
Boker A *(15)*								
SMU-578	Layer 1	charcoal		EUP	37920	2810	45699	39812
SMU-187**	Layer 1	charcoal		EUP	>33000			
SMU-260**	Layer 1	charcoal		EUP	>33420			
Kadesh Barnea (15)								
Pta 2819		ostrich eggshell		EUP	33800	940	39796	37421
Pta 2964		ostrich eggshell		EUP	32470	780	38187	36089
Boker Tachtit (this work)								
	Level							
RTD 7736	4	charcoal	ABA	IUP	41828	391	44904	44369
RTD 7739	4	charcoal	ABA	IUP	43972	610	46934	45665
RTD 7741	4	charcoal	ABA	IUP	44314	634	47316	45966

RTD 8163	2.1	charcoal	ABA	IUP	41713	419	44863	44280
RTD 8146	2.1	charcoal	ABA	IUP	43331	493	46110	45215
RTD 8158.1	2	charcoal	ABA	IUP	41299	390	44631	43971
RTD 8156	2	charcoal	ABA	IUP	41907	506	45070	44349
RTD 8164	2	charcoal	ABA	IUP	43461	503	46254	45279
RTD 8154	2	charcoal	ABA	IUP	44627	737	47687	46139
RTD 8147	2	charcoal	ABA	IUP	44987	464	47905	46762
RTD 8165	2	charcoal	ABA	IUP	45293	613	48267	46876
RTD 8155*	2	charcoal	ABA	IUP	47211	628	**50640**	**48633**
RTD 8161	2	charcoal	ABA	IUP	41310	396	44640	43974
RTD 8160.1	2	charcoal	ABA	IUP	43266	482	46050	45195
RTD 8149	2	charcoal	ABA	IUP	44017	532	46910	45790
RTD 8162.1*	**2**	charcoal	ABA	IUP	47039	744	**50574**	**48387**
RTD 7740	2	charcoal	ABA	IUP	46095	808	**49648**	**47581**
			OSL, TL, U-series, AAR					
Tor Faraj (15)								
	C	burnt flint	TL	LMP	52800	3000		
	C	burnt flint	TL	LMP	47500	3000		
	C	burnt flint	TL	LMP	43800	2000		
	C	ostrich eggshell	U-series	LMP	62400	14000		
	C	ostrich eggshell	U-series	LMP	28900	3900		
AAL-5739	C	ostrich eggshell	AAR	LMP	69000	6000		
Far'ah II (14)								
BE-12	Sq L2	quartz	OSL multigrain	LMP	**43000**	**3000**		
BE-12	Sq L2	quartz	OSL single grain	LMP	**47000**	**3000**		
BE-11	Sq H5	quatz	OSL multigrain	LMP	**43000**	**3000**		

BE-11	Sq H5	quartz	OSL single grain	LMP	**42000**	**3000**		
Wadi Aghar (15)	Layer							
gsj18225	B		OSL	IUP	39000	3000		
gsj18226	B		OSL	IUP	36000	3000		
gsj18223	C		OSL	IUP	45000	3000		
gsj17384	D1		OSL	IUP	41000	3000		
gsj18227	D1		OSL	IUP	42000	3000		
gsj18224	D1		OSL	IUP	45000	3000		
gsj17385	D2		OSL	IUP	50000	3000		
Boker Tachtit (this work)			OSL Quartz ky	±1σ	IRSL fading corr. ky	±1σ	Post IR-IRSL 290 ky	±1σ
L-EVA 1355	AH-A Below BG	OSL-2	51000	4000	44000	5000	59000	5000
L-EVA 1356	AH-A Above Level 4	OSL-3-1	41000	3000	41000	5000	52000	4000
L-EVA 1357	AH-A Above Level 4	OSL-4-1	48000	4000	42000	5000	45000	4000
L-EVA 1358	AH-B Below Level 4	OSL-6-1	43000	3000	39000	5000	45000	4000
L-EVA 1359	AH-B Between Level 2 and 4	OSL-7-1	58000	3000	52000	6000	54000	4000
L-EVA 1360	Above AH-B Level 2	OSL-8-2	42000	4000	44000	5000	50000	4000
L-EVA 1361	Below AH-B Level 2	OSL-9-1	53000	4000	49000	6000	52000	5000

Table SI-4. List of dates used for the chronological charts in figure 5. Sources from references (9-15) are indicated in the table. Samples are separated into two major groups based on the analytical method applied: 1 Radiocarbon and 2 OSL, TL, U-Series and AAR. Samples with * are beyond the 2020 calibration curve for the terrestrial (7) and

marine calibrations (16). ** are samples that were, due to analytical limitation, reported as > age and were not calibrated.

Figure SI-14: Bayesian Modelling

Several models have been tried using the Bayesian approach with different a priori assumptions. We present here only two extreme models following the stratigraphy and assuming the youngest sample in each context is the correct one (Figure SI-14A) or the oldest sample is the correct one (Figure SI-14B). Other approaches could be that, following the stratigraphy, averages are used or phases. In these cases one would have to choose which model is considered most appropriate, with the danger that this would introduce an unsubstantiated bias into the interpretation. Several models (e.g. general and charcoal outlier models) were tried. The overall agreement was very low for any of the models, with the charcoal outlier model almost impossible to run.

In conclusion, Boker Tachtit is one case where the use of modelling could have the undesired consequence of detracting from what appears to be the real problem, namely that some of the charcoal fragments analysed are not in situ and this might indicate yet unknown site formation processes.

A)

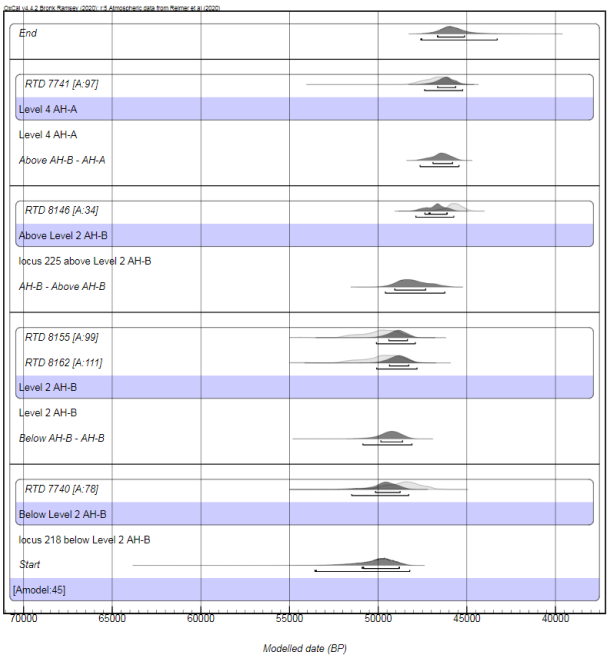

B)

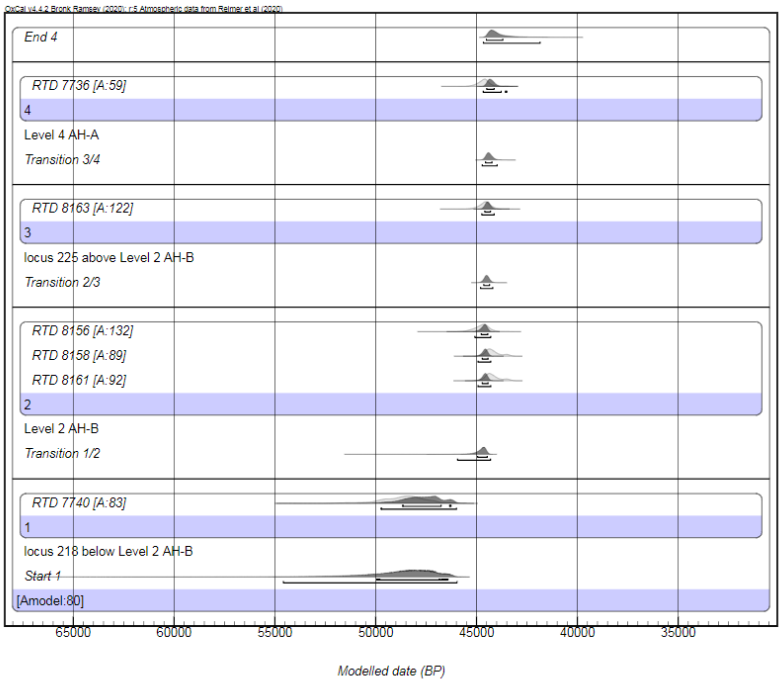

Figure SI-14. A) Bayesian sequence model assuming that the oldest dates in each level are the correct dates, B) Bayesian sequence model assuming that the youngest dates are the correct dates. These would represent two extreme interpretations of the chronostratigraphy with very different results. We have no criteria to justify choosing one or the other model or any intermediate model.

SI- 5. Luminescence dating (OSL)

Nineteen sediment samples were collected from the newly exposed section in 2013 (Fig. SI-15). We selected 10 of these and report the luminescence dating results obtained. Three of these samples were from the Bedded Gravel lithostratigraphic unit (BG) and seven were from the underlying silty sands unit (SSd) in Mark's section D. The sediment samples were collected by inserting steel tubes (diameter: 5cm, length: 20cm) into the cleaned sections.

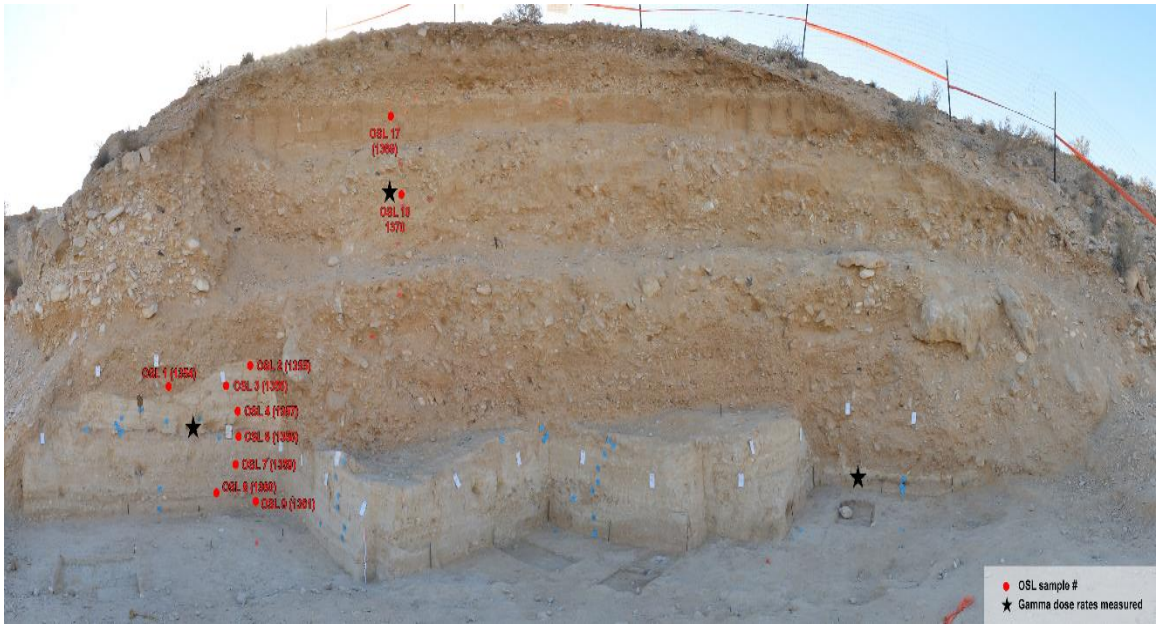

Figure SI-15. Boker Tachtit excavation view. The location of the OSL samples. Field numbers and lab numbers are shown. Archaeological Level 2 and Level 4 are between OSL samples 9-8 and 5-4 respectively.

Analytical strategy and instrumentation

The approach adopted in this study consists of combining the dating of quartz and feldspar in order to take advantage of their complementary characteristics. Contrary to the quartz, for which the internal dose rate is negligible, the internal potassium content of the feldspar makes them less dependent on micro environmental variations especially in contexts where the external dose rate is low. In addition, the different luminescence signals from quartz and feldspar measured at several temperatures, are characterized by different bleaching rates. A comparison of these rates allows for the identification or at least discussion of the state of bleaching in the samples (17,18,19).

In general, the analysis of coarse grains can be of interest for luminescence dating since 1) it is possible, after having etched the minerals, to avoid the external alpha contribution and 2) the internal dose rate of feldspar increases with the granulometric size of the grains. However, unsurprisingly, the coarser fraction (> 60µm) does not provide any feldspar and very few quartz grains, since the minerals in the silt fraction derive from aeolian sediments that have been locally reworked into the site by fluvial deposition. As a consequence, both quartz and feldspar grains were measured from the same granulometric fraction: 40-63 µm.

This grain size was selected by wet sieving and chemically treated with HCl and H_2O_2 in order to remove the carbonates and organic materials respectively. Then, the residual fraction was split into two parts. One part received an additional treatment with H_2SiF_6 to dissolve the silicates other than quartz. The other part was used for the feldspar measurements.

For the luminescence measurements, we mounted the grains in steel cups using silicone oil sprayed over a mask of 1 mm in diameter for the quartz and of 3 mm for the feldspar. We measured the samples on two Risø TL-DA-20 readers fitted with calibrated beta sources. We stimulated the quartz minerals using blue LEDs (470 nm) and detected the resulting signals with an EMI 9235QB photomultiplier through a 7.5 mm thick Hoya U-340 filter. For the feldspars, we used a combination of 870 nm IR diodes and a combination of Schott BG-39 and Schott BG-3 detection filter.

Dose rates

We assumed a 40K internal content of 12.5 ± 0.5% for the feldspar (20). For the quartz, it has been considered that the internal dose rate is negligible. For the determination of the external dose rate, the K, U, Th contents of the sediments were measured using high-resolution gamma spectrometry on the homogenized external part of the tubes. The 238U and 232Th decay series have been found to be at equilibrium at present day.

The external alpha, beta and gamma contributions to the dose rate have been calculated from conversion factors from Guérin et al. (2011) (21). Grain size attenuation factors were taken from Guérin et al. 2012 (22). The relative sensitivity of quartz to alpha rays compared to beta rays was assumed to be 5 µGy/103 alpha/cm2 (23) and an a-value of 0.08 ± 0.02 was taken into account for feldspar (24).

Due to the complexity of evaluating the mean water content of the sediments since deposition, this parameter usually represents a large part of the age uncertainties. In particular, the site of Boker Tachtit, located today in a semi-arid context, has most likely experienced major hydrometric variations. We assume here that the current water content is close to the moisture content over the burial time. We measured a water content of around 3% (percentage of dry mass) in three samples from the overlying gravels (BG) and a value of around 10% for the samples extracted from the silty sands unit (SSd). This difference between the two deposits fits with their respective granulometries (finer sediments can have higher moisture contents). Considering these data, we selected 6 ± 4 % as the water content for the BG sediments and 12 ± 8 % for the SSd deposits (Table SI-5). The calculated dose rates are reported in Table SI-5. The BG samples have slightly higher beta and gamma dose rates compared to the SSd samples. Within the two sediment packages, variation in the analyzed samples is low.

					external dose rates (Gy/ka)					internal dose rate (Gy/ka)	total dose rate (Gy/ka)	
					cosmic	alpha		beta	gamma	beta		
sample	water content (%)	K (%)	U (ppm)	Th (ppm)		Quartz	Feldspar			Feldspar	Quartz	Feldspar
L-EVA 1369	6 ± 4	0.76 ± 0.07	2.14 ± 0.26	4.70 ± 0.30	0.18 ± 0.02	0.13 ± 0.03	0.26 ± 0.05	0.96 ± 0.06	0.61 ± 0.03	0.11 ± 0.004	1.85 ± 0.07	2.01 ± 0.09
L-EVA 1370	6 ± 4	0.58 ± 0.06	2.46 ± 0.28	3.17 ± 0.21	0.15 ± 0.01	0.12 ± 0.03	0.25 ± 0.05	0.81 ± 0.06	0.53 ± 0.03	0.11 ± 0.004	1.61 ± 0.07	1.84 ± 0.08
L-EVA 1354	6 ± 4	0.54 ± 0.06	2.34 ± 0.29	3.19 ± 0.21	0.13 ± 0.01	0.12 ± 0.03	0.24 ± 0.05	0.77 ± 0.06	0.51 ± 0.03	0.11 ± 0.004	1.53 ± 0.07	1.76 ± 0.08
L-EVA 1355	12 ± 8	0.32 ± 0.04	2.22 ± 0.29	2.05 ± 0.15	0.17 ± 0.02	0.09 ± 0.02	0.19 ± 0.04	0.53 ± 0.04	0.31 ± 0.03	0.11 ± 0.004	1.10 ± 0.06	1.30 ± 0.07
L-EVA 1356	12 ± 8	0.35 ± 0.03	2.50 ± 0.30	2.32 ± 0.35	0.16 ± 0.02	0.10 ± 0.03	0.21 ± 0.05	0.59 ± 0.04	0.35 ± 0.03	0.11 ± 0.004	1.21 ± 0.06	1.42 ± 0.07
L-EVA 1357	12 ± 8	0.31 ± 0.03	2.40 ± 0.21	1.81 ± 0.12	0.15 ± 0.01	0.09 ± 0.02	0.19 ± 0.04	0.54 ± 0.03	0.32 ± 0.02	0.11 ± 0.004	1.11 ± 0.05	1.31 ± 0.06
L-EVA 1358	12 ± 8	0.55 ± 0.06	2.44 ± 0.24	4.00 ± 0.23	0.15 ± 0.01	0.12 ± 0.03	0.24 ± 0.05	0.76 ± 0.05	0.42 ± 0.02	0.11 ± 0.004	1.45 ± 0.06	1.68 ± 0.07
L-EVA 1359	12 ± 8	0.23 ± 0.02	1.78 ± 0.19	1.64 ± 0.11	0.14 ± 0.01	0.07 ± 0.02	0.15 ± 0.03	0.41 ± 0.03	0.25 ± 0.02	0.11 ± 0.004	0.87 ± 0.04	1.05 ± 0.05
L-EVA 1360	12 ± 8	0.31 ± 0.04	1.84 ± 0.25	2.08 ± 0.15	0.13 ± 0.01	0.08 ± 0.02	0.16 ± 0.04	0.47 ± 0.04	0.27 ± 0.03	0.11 ± 0.004	0.94 ± 0.05	1.05 ± 0.06
L-EVA 1361	12 ± 8	0.45 ± 0.04	1.84 ± 0.28	2.87 ± 0.20	0.13 ± 0.01	0.09 ± 0.02	0.18 ± 0.04	0.59 ± 0.04	0.31 ± 0.03	0.11 ± 0.004	1.12 ± 0.06	1.32 ± 0.06

Table SI-5: Dosimetric data associated with the luminescence samples.

The K, U, Th concentrations have been measured performing high-resolution gamma spectrometry on the homogenized external part of the tubes for each sample. The external dose rates are calculated from the moisture content reported in the second column.

As shown in TableSI-5, the gamma dose rates calculated from the K, U, Th contents of the sediment range between 0.51 ± 0.03 and 0.61 ± 0.03 Gy/ka for the BG samples and between 0.27 ± 0.03 and 0.42 ± 0.02 Gy/ka for the SSd samples. These results indicate that the gamma dose rate is roughly homogeneous within the two sediment types. In addition, we performed gamma measurements on site using a LaBr probe calibrated with the threshold technique (25). This method has the advantage of taking into account more of the dosimetric environment surrounding the dating samples. We acquired gamma spectra at the locations of three samples (gamma dose rate obtained: 0.60±0.01Gy/ka for L-EVA 1369, 0.46±0.01Gy/ka for L-EVA 1358, 0.32±0.01Gy/ka for L-EVA 1361). The gamma dose rates determined by two methods (field spectrometry versus K, U, Th measured from the sediment samples) are in good agreement, which suggests that the radioelement content determined from the external part of the sampling tubes is representative of the environment at a larger scale, and, therefore, is suitable for gamma dose rate determination.

We calculated cosmic dose rates using published data (26) and after having evaluated the mean depth of each sediment sample (Table SI-5). In this regard, we considered the samples from the two lithostratigraphic units BG and SSd separately. Since the BG can be considered as one single event, we used the present day depths of samples L-EVA 1368, L-EVA 1370 and L-EVA 1354 for the cosmic dose rate calculation. An erosional phase, perhaps significant in extent, separates the SSd from the BG meaning that the SSd deposit could have been thicker prior to this phase. We consider here that prior to erosion the SSd deposit was 50 cm thicker than what we observe today. We assign 10% uncertainties to the cosmic dose rate.

The total dose rates for both quartz and feldspar are given in Table SI-5. Overall, the total dose rate for feldspar minerals is 8%-21% higher in comparison to quartz. The beta dose, at around 50% of the total, represents the main contribution to the dose rates.

Equivalent Dose measurements (D_e)

Quartz

The fast component of the OSL signals was measured on quartz (Fig.SI-16) using a standard multi-grain SAR protocol (27,28).

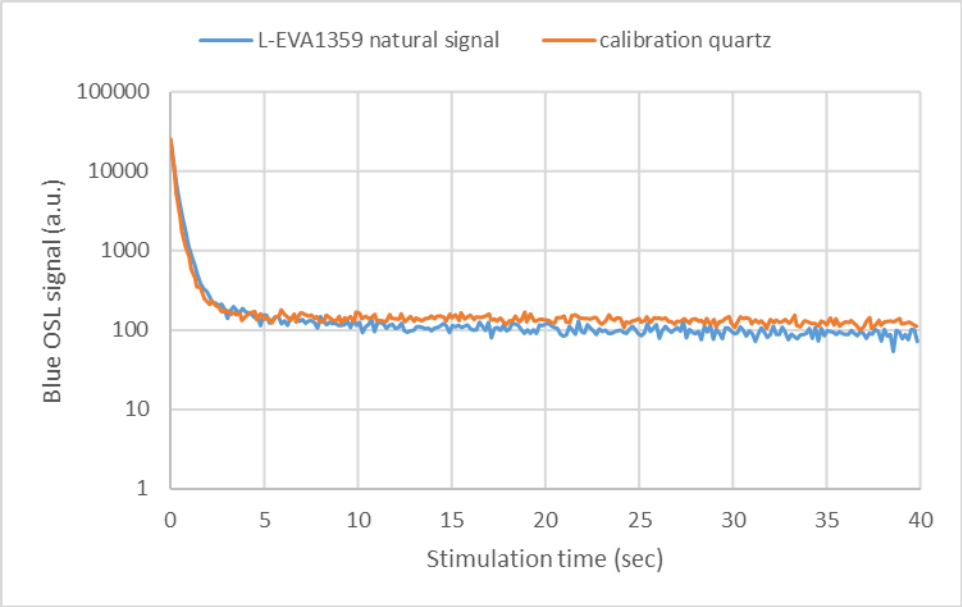

Figure SI-16. Natural OSL curve of L-EVA1359 measured using the same experimental conditions as a calibration quartz: after a PH260°C, 10s; stimulation blue LED at 125°C for 40s.

In order to check the stability of the natural signals, we performed preheat plateau tests for all samples. Fig. SI-17 shows the example of sample L-EVA 1370, which is typical of all other samples. Each point on the figure corresponds to the average of three aliquots; the cutheat before test dose measurement was kept constant (160°C), whereas the preheat temperature was varied from 220 to 280°C, by steps of 20°C. No trend could be observed as a function of preheat temperature. As a consequence, we choose for the following steps a PH260°C parameter.

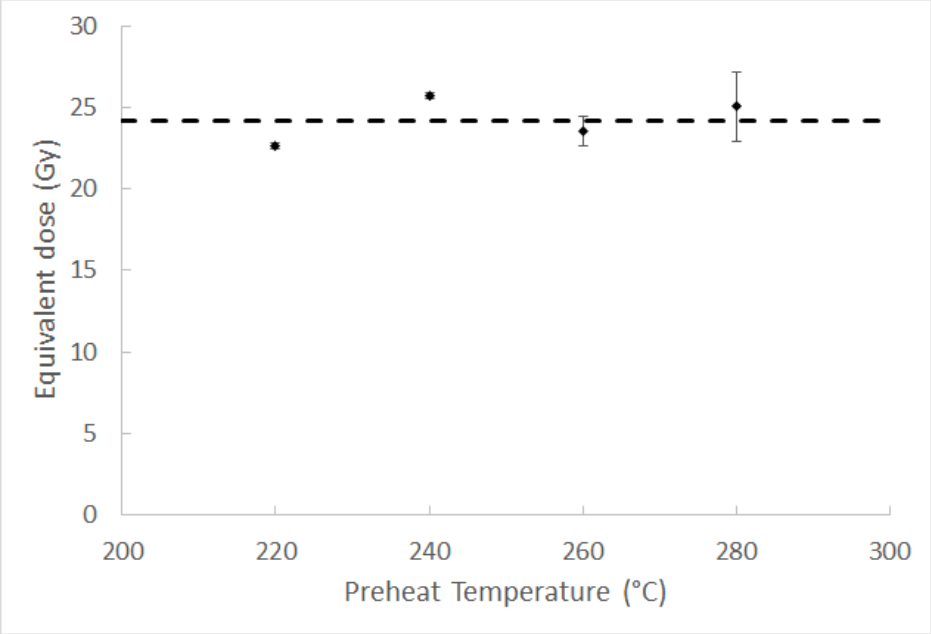

Figure SI-17. Equivalent doses resulting from preheat plateau test for sample L-EVA1370.

Dose recovery tests were performed to check the efficiency of the SAR protocol described in Table SI-6 to recover a known dose: 33Gy for the BG samples and 66Gy for the SSd samples.

For that purpose, we exposed 3 aliquots from each sample (except for sample L-EVA 1360, for which we could only prepare 2 aliquots) to light for 8 minutes in a solar simulator, and then delivered a known dose in the luminescence reader used for De determination. All dose recovery ratios were within 10 % of unity, and the average value was 0.98 +/- 0.01.

For the natural D_e determination, we measured 24 aliquots of quartz grains following the SAR protocol described in Table SI-6 and validated by previous preliminary tests. We derived the net signal intensities from the sum of the OSL in the first 0.8s minus a background calculated in the last 8s of the signal. We fitted regenerative growth curves using a single saturating exponential. The resulting D_e values are lower than $2 \times D_0$ value, which indicates that the accumulated doses are far from the saturation level of Boker Tachtit quartz (following equation: $L/T = A (1 - \exp(-D/D_0)$. D_0 corresponds to the curvature parameter of the saturating exponential, L/T is the normalised luminescence intensity, A corresponds to the maximum L/T value and D to the dose).

Even if they do not affect significantly the mean results, individual D_e values for which the measurements do not pass the recycling ratio criteria - that must fall within the 0.9-

1.1 range (1 aliquot for L-EVA 1359; 2 aliquots for L-EVA 13657 and 3 aliquots for L-EVA 1359) - have been excluded as a precaution.

For each sample, the mean D_e was then obtained calculating the plain arithmetic average for each sample (Table SI-6).

step	*(A) OSL SAR protocol*	*step*	*(B) $IRSL_{50}$ SAR protocol*	*step*	*(C) post IR-$IRSL_{290}$ SAR protocol*
1[a]	regenerative dose	1[a]	regenerative dose	1[a]	regenerative dose
2	Preheat to 260°C for 10s	2	Preheat to 250°C for 60s	2	Preheat to 320°C for 60s
3[b]	Stimulate with blue LEDs at 125°C for 40s	3[b]	Stimulate with infrared diodes at 50°C for 40s	3	Stimulate with infrared diodes at 50°C for 200s
4	Give test dose	4	Give test dose	4[b]	Stimulate with infrared diodes at 290°C for 200s
5	Preheat to 160°C for 10s	5	Preheat to 250°C for 60s	5	Give test dose
6[c]	Stimulate with blue LEDs at 125°C for 40s	6[c]	Stimulate with infrared diodes at 50°C for 40s	6	Preheat to 320°C for 60s
7[d]	Stimulate with blue LEDs at 280°C for 40s	7[d]	Stimulate with infrared diodes at 30°C for 300s	7	Stimulate with infrared diodes at 50°C for 200s
	return to step 1		return to step 1	8[c]	Stimulate with infrared diodes at 290°C for 200s
				9[d]	Stimulate with infrared diodes at 325°C for 100s
					return to step 1

Table SI-6: SAR protocols used in this study for the D_e determination of quartz protocol (A) and feldspar (protocols (B) and (C). (A) 0 dose is given at this step for the 1st cycle measurement of natural signal and for the 6th cycle of the SAR protocol. (B) Resulting luminescence signal corresponding to Ln or Lx depending on the step 1. (C) Normalization signal (Tn or Tx) induced by a fixed test dose. (D) Step applied to reset the signal at the end of each SAR cycle.

The dispersion of the equivalent doses beyond measurement uncertainties can be characterized by the overdispersion parameter of the Central Age Model (29). Here, the uncertainties assigned to each individual dose derive from the Poisson statistics and the fitting uncertainties. The resulting overdispersion range between 6 ± 1 % and 72 ± 11 % (Table SI-7). Sample L-EVA 1356, located on top of SSd in unit A, has a 72% overdispersion (see figure SI-17). This value is particularly high, especially considering the averaging effect of multi-grain measurements. Interestingly, two of the measured aliquots have D_e values around 4.5 Gy, which is 10 times lower than, and more than 4 standard deviations (when estimating this standard deviation without these two values) away from, the average equivalent dose (Figure SI-18) despite the fact that they pass the sample acceptance criteria. It would have been interesting to have this information at a single grain resolution; however, the quantity of grains in the appropriate size fraction was not sufficient to perform this kind of analysis. When those two aliquots are excluded, the overdispersion becomes very low (2 ± 7 %) and the mean D_e is 52 ± 2 Gy for an age of 43 ± 3ka against 48 ± 3 Gy for an age of 40 ± 3ka when taking all aliquots into account. For the final age calculation, we use the first value (excluding the two low dose aliquots).

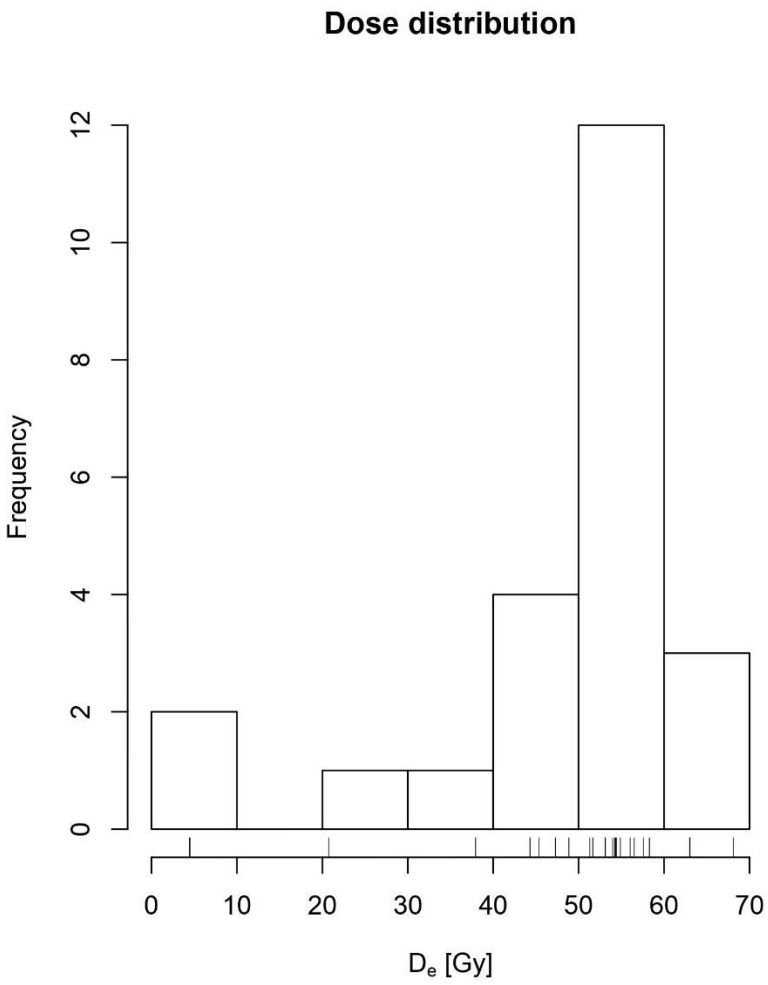

Figure SI-18: Distribution of dose of sample L-EVA 1356

Feldspar

It is well known that the feldspar luminescence signal is characterized by an athermal instability, called anomalous fading (31,32), which requires measuring and applying a fading correction factor to obtain reliable ages (31). Thomsen et al. (34) report alternative methods to reduce and even bypass this fading problem in measuring the postIR-IRSL signal at elevated temperatures. In particular, it has been shown (35,36) that the De resulting from the IRSL signal measured at 290°C after a first IRSL stimulation at 50°C does not need a fading correction. However, this signal is characterized by a much slower bleaching rate in comparison to the conventional IRSL signal measured at 50°C. This means that the minerals need to be exposed to sunlight longer in order to completely

erase any pre-existing signal prior to deposition. Considering the advantages and weaknesses of $IRSL_{50}$ and postIR $IRSL_{290}$, we decided to perform both techniques and to compare the results for all samples. In both cases, we performed SAR protocols on 12 aliquots per sample following the steps described in Table SI-6.

We derived the net signal intensities from the sum of the IRSL and postIR-IRSL in the first 2.4s minus a background calculated in the last 8s and 40s of the IRSL and postIR-IRSL signals respectively. We fitted regenerative growth curves using a single saturating exponential. The resulting overdispersions, fall between 0 and 20 ± 4 %, are overall lower than for the quartz, even including sample L-EVA 1356 for which the high overdispersion was discussed above (Table SI-7).

Unsurprisingly, due to the fading phenomenon, the D_e determined by measuring the $IRSL_{50}$ signal are lower than those coming from the postIR-$IRSL_{290}$. We measured the fading rates following the approach developed by Huntley and Lamothe (33). For that purpose, the 12 aliquots that were used to determine the D_e were bleached for 1 hour in a solar simulator prior to the fading measurements. The obtained fading rates are reported in Table SI-7 and do not show any significant variation between samples (3.2-3.7 %/decade).

We measured the residual doses of three modern samples coming from the channel of Nahal Zin river in front of the site. From geoarchaeological and micromorphological studies, the SSD complex is mostly related to water laid sediments under low energy depositional environments. The modern sediments sampled, should reflect a similar sedimentary catchment as the one expected for the time of the formation of the deposits at Boker Tacthit. The BG layers above the SSD complex are also water lain, but reflect higher energy deposits. The three modern samples are characterized by different grain sizes: fine sands, medium sands and coarse sands. Based on the measurements of the natural postIR-IRSL signals of 12 aliquots/sample, we obtained respectively a dose of 12±Gy, 9±3Gy and 11±2 Gy. Since, the three samples provide compatible results, we used the mean value of 11Gy that has been subtracted to the De postIR-IRSL (see impact on the ages in SI-7d).

	Quartz				*Feldspar*									
sample	*total dose rate (Gy/ka)*	*D_e OSL (Gy) [a]*	*OD (%)*	***Age OSL (ka)***	*total dose rate (Gy/ka)*	*D_e IRSL$_{50}$ (Gy) [b]*	*OD (%)*	***Age IRSL$_{50}$ (ka): fading uncorr.***	*g-value (%/decade) [c]*	***Age IRSL$_{50}$ (ka): fading corr.***	*D_e post IR-IRSL290 (Gy) [b]*	*OD (%)*	***Age postIR-IRSL$_{290}$***	***Age postIR-IRSL$_{290}$ - residual (ka) [d]***
L-EVA 1369	1.85 ± 0.07	27 ± 1	17 ± 3	**15 ± 1**	2.01 ± 0.09	25 ± 1	3 ± 1	**12 ± 1**	3.4 ± 0.8	**17 ± 2**	42 ± 1	3 ± 2	**20 ± 1**	**15 ± 1**
L-EVA 1370	1.61 ± 0.07	25 ± 1	16 ± 3	**15 ± 1**	1.84 ± 0.08	21 ± 1	9 ± 2	**12 ± 1**	3.5 ± 0.8	**16 ± 2**	37 ± 1	0	**20 ± 1**	**14 ± 1**
L-EVA 1354	1.53 ± 0.07	26 ± 2	37 ± 5	**17 ± 2**	1.76 ± 0.08	23 ± 1	2 ± 2	**13 ± 1**	3.3 ± 0.8	**18 ± 2**	40 ± 3	20 ± 4	**23 ± 2**	**16 ± 2**
L-EVA 1355	1.10 ± 0.06	56 ± 2	16 ± 3	**51 ± 4**	1.30 ± 0.07	42 ± 1	0	**32 ± 3**	3.2 ± 0.8	**44 ± 5**	76 ± 2	7 ± 2	**59 ± 5**	**50 ± 5**
L-EVA 1356	1.21 ± 0.06	48 ± 3	72 ± 11	**40 ± 3**	1.42 ± 0.07	42 ± 1	3 ± 1	**30 ± 2**	3.4 ± 0.8	**41 ± 5**	74 ± 1	4 ± 1	**52 ± 4**	**45 ± 4**
	1.21 ± 0.06	52 ± 2	2 ± 7	**43 ± 3**										
L-EVA 1357	1.11 ± 0.05	53 ± 1	12 ± 2	**48 ± 4**	1.31 ± 0.06	40 ± 1	5 ± 1	**30 ± 2**	3.3 ± 0.8	**42 ± 5**	59 ± 2	10 ± 2	**45 ± 4**	**36 ± 4**
L-EVA 1358	1.45 ± 0.06	63 ± 1	6 ± 1	**43 ± 3**	1.68 ± 0.07	47 ± 1	2 ± 2	**28 ± 2**	3.3 ± 0.8	**39 ± 5**	75 ± 1	5 ± 1	**45 ± 4**	**38 ± 4**
L-EVA 1359	0.87 ± 0.04	51 ± 2	12 ± 2	**58 ± 5**	1.05 ± 0.05	40 ± 2	12 ± 3	**38 ± 2**	3.1 ± 0.8	**52 ± 6**	57 ± 1	4 ± 1	**54 ± 4**	**43 ± 4**
L-EVA 1360	0.94 ± 0.05	40 ± 2	21 ± 3	**42 ± 4**	1.05 ± 0.06	34 ± 1	7 ± 2	**32 ± 3**	3.1 ± 0.8	**44 ± 5**	53 ± 1	0	**50 ± 4**	**40 ± 4**
L-EVA 1361	1.12 ± 0.06	60 ± 2	12 ± 2	**53 ± 4**	1.32 ± 0.06	45 ± 1	2 ± 2	**34 ± 3**	3.7 ± 0.8	**49 ± 6**	69 ± 3	12 ± 3	**52 ± 5**	**44 ± 5**

Table SI-7. Luminescence age results. The mean D_e values reported in this table correspond to the average of the individual values obtained for each aliquot. The associated errors are given by the standard deviation divided by the square root of the number of aliquots. a) The mean D_e reported correspond to the average of 24 aliquots except for samples L-EVA 1354, L-EVA 1355, L-EVA 1358, L-EVA 1360 (23 aliquots); L-EVA 1357 (22 aliquots) and L-EVA 1359 (21 aliquots) due to the rejection criteria (recycling out of 0.9-1.1 range). Two results are reported for L-EVA1356: before (40±3ka) and after subtraction of the two outliers (43±3ka). b) The mean D_e reported correspond to the average of 12 aliquots. c) Mean g value measured for the 12 aliquots used for the D_e determination. d) Ages calculated after having subtracted 11 Gy (measured on modern analogous samples) to the total dose determined. The discrepancy between the uncertainty quoted for the age and the quadratic sum of the uncertainties on the equivalent dose and dose rate comes from the addition, to the latter sum, of calibration uncertainties: 10% on concentrations in K, U and Th, and 1.5% on the laboratory source dose rate.

References

1. A. E. Marks, *Prehistory and Paleoenvironments in the Central Negev, Israel: the Avdat/Aqev Area (Vol. 3)*. (SMU Press 1983).
2. P. Goldberg, Geology of sites Boker and Boker Tachtit and their surroundings in Prehistory and paleoenvironments in the Central Negev, Israel, A. Marks, Ed. (SMU Press 1983) pp. 39-61.
3. Z. Stepka, O. Barzilai, S. Weiner, E. Boaretto, Microflint in archaeological sediments from Boker Tachtit, Israel: A new method for quantifying concentrations of small flint fragments. J. Archaeol. Sci. **91**, 52-64, (2018).
4. M. Goder-Goldberger, S. Weiner, O. Barzilai, E. Boaretto, Heating of flint artifacts from the site of Boker Tachtit (Israel) was not detected using FTIR peak broadening. J. Archaeol. Sci. Reports, **12** 173-182, (2017).

5. N.R. Rebollo, S. Weiner, F. Brock, L. Meignen, P. Goldberg, A. Belfer-Cohen, O. Bar-Yosef, E. Boaretto, New radiocarbon dating of the transition from the Middle to the Upper Paleolithic in Kebara Cave, Israel. J. Archaeol. Sci. **38** 2424-2433 (2011).
6. Regev, L., Steier, P., Shachar, Y., Mintz, E., Wild, E.M., Kutschera, W. and Boaretto, E., 2017. D-REAMS: A new compact AMS system for radiocarbon measurements at the Weizmann Institute of Science, Rehovot, Israel. Radiocarbon, ***59***, 775-784.
7. P.J. Reimer, W.E.N. Austin, E. Bard, A. Bayliss, P.G. Blackwell, C.B. Ramsey, M. Butzin, H. Cheng, R.L. Edwards, M. Friedrich, P.M. Grootes, T.P. Guilderson, I. Hajdas,T.J. Heaton, A.G. Hogg, K.A. Hughen, B. Kromer, S.W. Manning, R. Muscheler, J.G. Palmer, C. Pearson, J.v.d. Plicht, R.W. Reimer,D.A. Richards, E.M. Scott, J.R. Southon, C.S.M. Turney, C.S.M., L. Wacker, F. Adolphi, U. Büntgen, M. Capano, S. Fahrni, A. Fogtmann-Schulz, R. Friedrich, S. Kudsk, F. Miyake, J. Olsen, F. Reinig, M. Sakamoto, A. Sookdeo, S. Talamo, The IntCal20 Northern Hemisphere radiocarbon calibration curve (0-55 cal kBP). Radiocarbon, **62,** 725-758 (2020).
8. M. Stuiver, H. A. Polach. Discussing reporting C-14 data. Radiocarbon **19**, 355-363 (1977).
9. S. L. Kuhn, M. C. Stiner, E. Güleç, I. Özer, H. Yilmaz, I. Baykara, A. Açikkol, P. Goldberg, K. M. Molina, E. Ünay, F. Suata-Alpaslan, The early Upper Paleolithic occupations at Üçağizli Cave (Hatay, Turkey). J. Hum. Evol. **56,** 87–113 (2009).
10. K. Douka, Exploring "the great wilderness of prehistory": the chronology of the Middle to the Upper Paleolithic Transition in the Northern Levant. Mitteilungen der Gesellschaft für Urgeschichte, **22**, pp.11–40 (2013).
11. K. Douka, C. A. Bergman, R. E. Hedges, F. P. Wesselingh, T. F. Higham, Chronology of Ksar Akil (Lebanon) and implications for the colonization of Europe by anatomically modern humans. PloS one **8**, e72931 (2013).
12. M. D. Bosch, M. A. Mannino, A. L. Prendergast, T. C. O'Connell, B. Demarchi, S. M. Taylor, L. Niven, J. v.d Plicht, J.-J. Hublin New chronology for Ksâr 'Akil (Lebanon) supports Levantine route of modern human dispersal into Europe. Proc. Natl. Acad. Sci. U.S.A. **112**, 7683-7688 (2015).
13. B. Alex, O. Barzilai, I. Hershkovitz, O. Marder, F. Berna, V. Caracuta, T. Abulafia, L. Davis, M. Goder-Goldberger, R. Lavi, E. Mintz, L. Regev, D. Bar-Yosef Mayer, J.-M. Tejero, R. Yeshurun, A. Ayalon, M. Bar-Matthews, G. Yasur, A. Frumkin, B. Latimer, M. G. Hans, E. Boaretto, Radiocarbon chronology of Manot Cave, Israel and Upper Paleolithic dispersals Science Advances, **3**, 11 e1701450 DOI: 10.1126/sciadv. (2017).
14. M. Goder-Goldberger, O. Crouvi, A. Ayalon, V. Caracuta, L. Kolska Horwitz, F. H. Neumann, N. Porat, T. Zilberman, E. Boaretto The Middle to Upper Paleolithic transition in the Southern Levant: New insights from the Late Middle Paleolithic site of Far'ah II, Israel Quaternary Science Reviews **237** 106304 (2020).
15. S. Kadowaki, Issues of chronological and geographical distributions of Middle and Upper Palaeolithic cultural variability in the Levant and implications for the learning behavior of Neanderthals and Homo sapiens in *Dynamics of Learning in Neanderthals and Modern Human*s, T. Akazawa, Y. Nishiaki, K. Aoki Eds., (Springer 2013) pp. 59-91.
16. T.J. Heaton, P. Köhler, M. Butzin, E. Bard, R.W. Reimer, W.E.N. Austin, C. Bronk Ramsey, Grootes, P.M., Hughen, K.A., Kromer, B., Reimer, P.J., Adkins, J.F., Burke, A., Cook,

M.S., J. Olsen, and L.C. Skinner, Marine20 the marine radiocarbon age calibration curve (0-55,000 cal BP). Radiocarbon, **62,** 779-820 (2020).
17. A. S. Murray, K. J. Thomsen, N. Masuda, J. P. Buylaert, M. Jain, Identifying well-bleached quartz using the different bleaching rates of quartz and feldspar luminescence signals. Radiation Measurements, **47**, 688-695 (2012).
18. D. I., Godfrey-Smith, D. J. Huntley, W. H. Chen, Optical dating studies of quartz and feldspar sediment extracts. Quaternary Science Reviews, **7**, 373-380 (1988).
19. J. P. Buylaert, M. Jain, A. S. Murray, K. J.Thomsen, C. Thiel ,R. Sohbati, A robust feldspar luminescence dating method for Middle and Late Pleistocene sediments. Boreas, **41**, 435-451 (2012).
20. D.J. Huntley, M.R. Baril, The K content of the K-feldspars being measured in optical dating or in thermoluminescence dating. Ancient TL. **15**, 11-13 (1997).
21. G. Guérin, N. Mercier, G. Adamiec, Dose-rate conversion factors: update. Ancient TL 29, 5-8 (2011).
22. G. Guérin, N. Mercier, R. Nathan, G. Adamiec, Y. Lefrais, On the use of the infinite matrix assumption and associated concepts: a critical review. Radiation Measurements **47**, 778-785 (2012).
23. C. Tribolo, D. Mercier, H. Valladas, Alpha sensitivity determination in quartzite using an OSL single aliquot procedure. Ancient TL **19**, 47-50 (2001).
24. J. Rees-Jones, Optical dating of young sediments using fine-grain quartz. Ancient TL **13**(2), 9-14 (1995).
25. G. Guérin, N. Mercier, Determining gamma dose rates by field gamma spectroscopy in sedimentary media: results of Monte Carlo simulations. Radiation Measurements **46**, 190-195 (2011).
26. J.R. Prescott, J.T. Hutton, Cosmic ray and gamma ray dosimetry for TL and ESR. Nucl. Tracks. Radiation Measurements **14**, 223-22 (1988).
27. A.S. Murray, A.G. Wintle, Luminescence dating of quartz using an improved single-aliquot regenerative-dose protocol. Radiation Measurements **32**, 57-73 (2000).
28. A.S. Murray, A.G. Wintle, The single-aliquot regenerative-dose protocol: potential for improvements in reliability. Radiation Measurements **37**, 377-381 (2003).
29. R. F. Galbraith, R. G. Roberts, G. M. Laslett, H. Yoshida, J. M. Olley, Optical dating of single and multiple grains of quartz from Jinmium rock shelter, northern Australia: Part I, experimental design and statistical models. Archaeometry, **41**, 339-364 (1999).
30. K. J. Thomsen, A. S. Murray, L. Bøtter-Jensen, Sources of variability in OSL dose measurements using single grains of quartz. Radiation Measurements, *39*, 47-61 (2005).
31. A.G. Wintle, Anomalous fading of thermoluminescence in mineral samples. Nature **245**, 143-144 (1973).
32. N.A. Spooner, The anomalous fading of infrared-stimulated luminescence from feldspar. Radiation measurements **23**, 625-632 (1994).
33. D.J. Huntley, M. Lamothe, Ubiquity of anomalous fading in K-feldspar and the measurement and correction for it in optical dating. Canadian Journal of Earth Sciences **38**, 1093-1106 (2001).

34. K. J. Thomsen, A. S. Murray, M. Jain, L. Bøtter-Jensen, Laboratory fading rates of various luminescence signals from feldspar-rich sediment extracts. Radiation measurements, ***43***, 1474-1486 (2008).
35. C. Thiel, J.P. Buylaert, A.S. Murray, B. Terhorst, I. Hofer, S. Tsukamoto, M. Frechen, Luminescence dating of the Stratzing loess profile (Austria)-testing the potential of an elevated temperature post-IR IRSL protocol. Quaternary International 234, 23-31 (2011).
36. J.-P. Buylaert, J. Mayank, A.S. Murray, K.J. Thomsen, C. Thiel, R. Sohbati, A robust feldspar luminescence dating method for Middle and Late Pleistocene sediments. Boreas 41, 435-451 (2012).